Vilniaus universitetas
Fizikos fakultetas
Teorinės fizikos ir astrofizikos institutas

Ravana Sadikhli

CHEMODINAMINĖS SAULĖS APLINKOS ŽVAIGŽDŽIŲ SAVYBĖS

MAGISTRO STUDIJŲ MOKSLINIS TIRIAMASIS DARBAS

Teorinės fizikos ir astrofzikos studijų programa

Studentė Ravana Sadikhli

Darbo vadovas dr. Šarūnas Mikolaitis

Instituto direktorius prof. Egidijus Anisimovas

Vilnius 2026

Vilnius university
Faculty of Physics
Institute of Theoretical Physics and Astronomy

Ravana Sadikhli

CHEMODYNAMIC PROPERTIES OF STARS IN THE SOLAR NEIGHBOURHOOD

MASTERS THESIS

Theoretical Physics and Astrophysics study programme

Student	Ravana Sadikhli
Thesis supervisor	dr. Šarūnas Mikolaitis
Director of institute	prof. Egidijus Anisimovas

Vilnius 2026

Abstract

We present a chemo-dynamical study of 110 stars in the Solar neighbourhood based on high-resolution spectroscopy and orbital modelling. Stellar atmospheric parameters ($T_{\rm eff}$, $\log g$, [Fe/H], and ξ) and α-element abundances were derived using standard spectroscopic methods. Radial velocities were determined via cross-correlation, and Galactic orbits were computed using the `galpy` package in an axisymmetric Milky Way potential. The sample spans metallicities in the range $-0.44 \leq [\mathrm{Fe/H}] \leq +0.03$ dex and includes both dwarf and giant stars, predominantly associated with the Galactic thin disk. We find a negative vertical metallicity gradient of $\mathrm{d[Fe/H]/d}Z_{\rm max} = -0.095 \pm 0.027$ dex kpc^{-1}, while the radial gradient is weak and not statistically significant. The dispersion in metallicity at a given orbital parameter suggests the presence of both thin- and thick-disk populations and indicates that radial migration and population mixing play an important role in shaping the local chemo-dynamical structure of the Milky Way.

Pateikiamas 110 žvaigždžių Saulės aplinkoje chemo-dinaminis tyrimas, pagrįstas didelės skiriamosios gebos spektroskopija ir orbitų modeliavimu. Žvaigždžių atmosferos parametrai ($T_{\rm eff}$, $\log g$, [Fe/H] ir ξ) bei α elementų gausos buvo nustatyti taikant standartinius spektroskopinius metodus. Radialiniai greičiai buvo apskaičiuoti kryžminės koreliacijos metodu, o Galaktikos orbitos – naudojant `galpy` paketą ašinės simetrijos Paukščių Tako potenciale. Tiriamasis imtis apima metalingumo intervalą $-0.44 \leq [\mathrm{Fe/H}] \leq +0.03$ dex ir sudaryta iš nykštukių bei milžinių žvaigždžių, daugiausia priklausančių Galaktikos plonajam diskui. Nustatytas neigiamas vertikalus metalingumo gradientas $\mathrm{d[Fe/H]/d}Z_{\rm max} = -0.095 \pm 0.027$ dex kpc^{-1}, tuo tarpu radialinis gradientas yra silpnas ir statistiškai nereikšmingas. Metalingumo sklaida esant tam pačiam orbitiniam parametrui rodo tiek plonojo, tiek storojo disko populiacijų egzistavimą bei leidžia daryti išvadą, kad radialinė migracija ir populiacijų maišymasis yra svarbūs formuojant vietinę Paukščių Tako chemo-dinaminę struktūrą.

Contents

Introduction

The physical and chemical characteristics of stars cannot be studied without the study of stellar spectra. Spectral lines are crucial in determining some of the important atmospheric parameters such as effective temperature, surface gravity, metallicity, and microturbulent velocity among others (Gray, 2005) These parameters are essential in establishing other properties of the stars such as mass, radius and luminosity and in classifying stars and their evolution.

Chemical abundances and analysis of chemical evolution of the Galaxy can also be determined using accurate atmospheric parameters and can be studied (Bensby et al., 2014; Chiappini et al., 1997). They can also be used to characterize stars that can contain planetary systems

Nevertheless, even bright stars in the neighbourhood of the Sun are not investigated thoroughly. It is demonstrated that not more than 30 percent of F5 and cooler dwarf stars with V less than 8 mag have been studied in detail through spectroscopic analysis (Mikolaitis et al., 2018). Surveys of spectroscopy, like the Gaia-ESO survey and APOGEE survey, are usually studied on fainter stars, and there are no bright close stars that are enough studied.

Besides chemical characteristics, stellar kinematics are also crucial in terms of the Milky Way galaxy structure. Stellar motions represent Galactic gravitational potential and may be applied to derive orbital parameters, including the eccentricity and vertical motions (Anders et al., 2014; Boeche et al., 2013; Mikolaitis et al., 2018).

The Section 1 of this work presents the methods of the delivery of atmospheric parameters, chemical abundance and orbital parameters of 110 stars. We used spectra of the 1.65-meter telescope in the Molėtai Astronomical Observatory and the VUES spectrograph to acquire the spectroscopic data with the telescope (Jurgenson et al., 2016) together with calculation of stellar orbits. In Section 2 overviews results and compares to other studies and the Section 3 provides summary and conclusions of the work.

Aims and Tasks

The aim of this research is to focus on exploring the chemical composition and atmospheric parameters of a sample of 110 stars in the Solar neighbourhood, as well as the analysis of their orbital periods in the Galactic disk.

The main tasks of this study are:

- To determine the equivalent widths (EWs) of a set of spectral lines with ARES software.
- To calculate the atmospheric parameters, such as effective temperature (T_{eff}), surface gravity ($\log g$), metallicity ([Fe/H]) and microturbulent velocity (ξ), on the basis of spectroscopic analysis, model atmospheres of MOOG.
- To measure the abundances of the elements of the group of alpha (Si, Ca, Ti) and Al, Sc and to test their dependence on the excitation potential and reduced equivalent width to confirm the consistency of the parameters derived.

- To determine radial velocities with the cross-correlation technique.
- Prepare astrometric and kinematic data, convert them to a Galactocentric frame of reference, and then calculate stellar orbits with the help of the Python package `galpy`.
- To derive the orbital parameters, such as eccentricity, pericentre and apocentre distance, mean Galactocentric radius and maximum height above Galactic plane.
- To measure the distributions of orbital parameters and cross these with spectroscopic metallicities and elemental abundances to study chemo-dynamical trends in the Solar neighbourhood.

1 Methods

This section explains the methodology that was used in the current study. The analysis was based on high-resolution spectroscopic observations which were then succeeded by measurements of the equivalent widths of absorption-lines and calculation of the stellar atmospheric parameters and chemical abundances. Standard methods, such as the use of model atmospheres, and the assumption of local thermodynamic equilibrium were used in the spectroscopic analysis.

Moreover, to examine the kinematic and orbital characteristics of the stars, the data of astrometric and radial-velocity were used. These measurements gave us orbital motions and to locate the stars in the Galactic context. The steps of the process, such as data reduction, determination of parameters and estimation of uncertainty, are introduced in detail in subsequent subsections.

1.1 Observations

We used spectra from archive of 1.65 m telescope at the Moletai Astronomical Observatory of Vilnius University in Lithuania, which is equipped with the high-resolution Vilnius University Echelle Spectrograph. This spectrograph provides wavelength coverage from 400 to 900 nm with $R \sim 36{,}000$, $R \sim 51{,}000$, and $R \sim 68{,}000$ resolution modes. For our work, we used the $R \sim 68{,}000$ mode for M spectral type stars and the $R \sim 36{,}000$ mode for other objects. Exposure times ranged between 900 and 2400 seconds, and the signal-to-noise ratios (S/Ns) varied between 75 and 200, with a median value of 96, depending on stellar magnitudes. Mikolaitis et al. (2018)

1.2 Stellar Atmospheric parameters and Chemical Abundance Analysis

A model atmosphere is an account of the physical properties in the outermost layers of the star which forms the observed spectrum. It gives the temperature, pressure, density, and opacity changes with depth, which are required in spectroscopic analyses and the calculation of abundances (Gray, 2005; Gustafsson et al., 2008).

In this work, MARCS model atmospheres were used (Gustafsson et al., 2008). These are one-dimensional hydrostatic models which are determined under the condition of local thermodynamic equilibrium and conservation of fluxes.

All MARCS model atmospheres are consist of a series of depth layers which model the change in physical quantities across the stellar atmosphere. Parameters in every layer are the temperature, gas pressure, electron pressure, density and the opacity. The grid has been extended to cover a variety of effective temperatures, surface gravities, metallicities, and chemical compositions (e.g., enhancement of the elements of the alphas), and enables building of appropriate model atmospheres by interpolation.

1.2.1 Measurement of Equivalent Width and Line Selection

In stellar astronomy, one of the most important quantities is the equivalent width (EW) which measures the strength of a spectral lines. It is the width of a rectangle whose area is that of the absorption line and the height is that of the continuum level. This parameter is a quantitative measure of the amount of the light, which is absorbed at a particular wavelength and has direct connection to the abundance of elements in the stellar atmosphere being tested-bsased on a specific wavelength Gray (2005).

The equivalent widths in this work were calculated using ARES package. It is a tool that can be used to extract major parameters of lines Sousa et al. (2007). After the measurements of ARES, the data were converted to MOOG via a tailored python script. The script compared the wavelengths of the ARES output to the lines known in the MOOG linelist and only the matches were kept in the final file to be used in the calculations of the abundances. To get a better understanding of how spectral lines are calculated manually and compare them with ARES measurements, the equivalent width of spectral lines of one of the stars was estimated using the Spectral Analysis Tool SPLAT-VO Instrument Figure 1, which is offered by the German Astrophysical Virtual observatory Škoda et al. (2014).

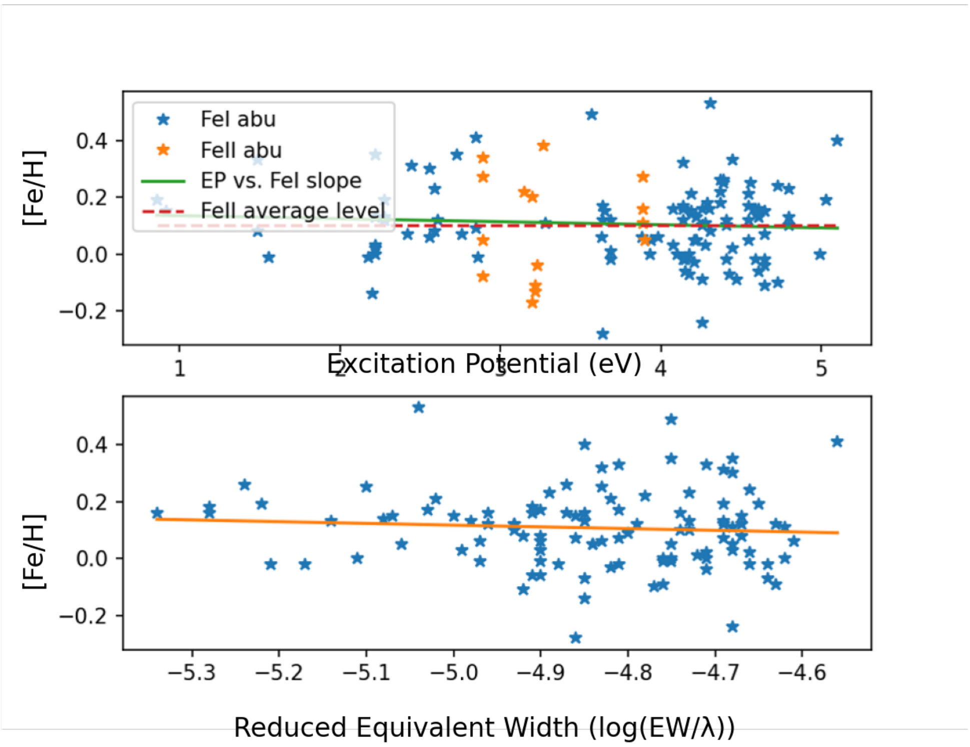

Figure 1 Iron abundances as a function of excitation potential and reduced equivalent width for the sample stars

Figure 2 and Figure 3 present example high-resolution spectra of the sample stars in the 6000–6100 Å region.

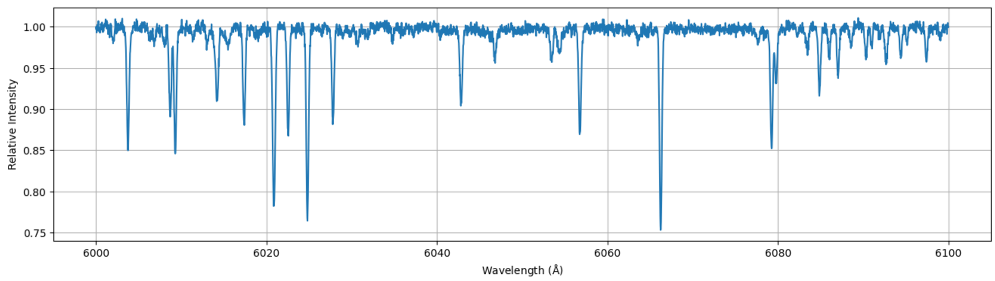

Figure 2 High-resolution spectrum of TYC 1383-84-1 in the wavelength range 6000–6100 Å, showing relative intensity as a function of wavelength.

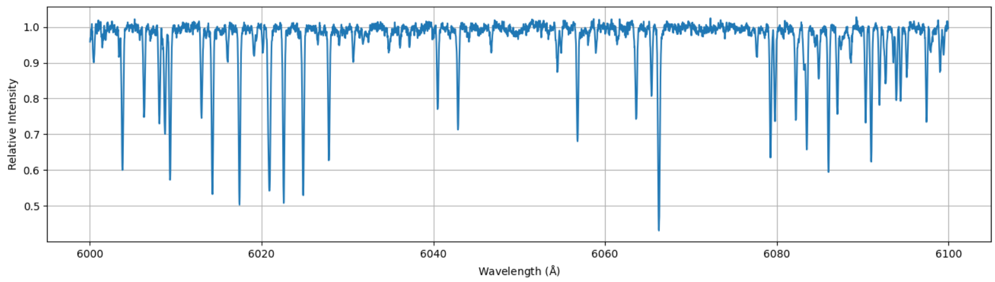

Figure 3 High-resolution spectrum of TYC 3425-1596-1 in the wavelength range 6000–6100 Å, showing relative intensity as a function of wavelength.

1.2.2 Effective temperature

The effective temperature, or T_{eff}, of a star, the temperature of a blackbody that would have the same total flux as the star, is one of the key parameters used to characterize atmospheres of stars. This has to do with the radiance of a star and radius in respect of the Stefan-Boltzmann law:

$$T_{\text{eff}} = \left(\frac{L}{4\pi R^2 \sigma}\right)^{1/4}$$

The method of the excitation equilibrium was used to measure the effective temperature in this work. The principle of this technique is the examination of Fe I abundance for every spectral lines with respect to excitation potentials. The temperature was adjusting until the slope of the relation between abundance of iron and excitation potential was near to zero so that the obtained abundances were not dependent on excitation potential anymore (Sousa et al., 2010). The slope of this relation is the change of the derived abundances with respect to excitation potential. The slope is non-zero, which means that there is a systematic dependence of abundance on excitation potential, whereas a slope near zero means that the excitation equilibrium is established and the effective temperature is obtained correctly. The linear association between two variables can be written as.

$$y = mx + b,$$

where m is the slope of the relation, i.e. the rate of change of y with respect to x and b is the intercept, i.e. the value of y at $x = 0$.

1.2.3 Surface gravity

Stellar surface gravity is to be the acceleration due to gravity at the star surface and it is one of the important parameters used to describe stellar atmospheres. It is defined as

$$g = \frac{GM}{R^2}$$

and where, G is the gravitational constant, and M is the mass of the stars, and R is the radius of the stars:

$$\log g = \log\left(\frac{M}{M_\odot}\right) - 2\log\left(\frac{R}{R_\odot}\right) + \log g_\odot$$

The ionization equilibrium was used to determine the surface gravity in this work. The rationale behind this approach is the comparative analysis of the average abundances as obtained with Fe I and Fe II spectral lines. The abundances were derived with the help of equivalent widths of these lines and calculation of elemental abundances with the help of stellar atmosphere models. The best value of log g was obtained by bringing the abundances obtained using Fe I and Fe I lines into agreement, a process that showed the ionization equilibrium (Hekker et al., 2013) . The process facilitates consistency of neutral and ionized species and gives a good approximation of the surface gravity. The last value of the log g is the one at which the ratio between the abundance of Fe I and Fe II is minimized. This technique has many applications in spectroscopic studies and offers strong surface gravity measurements when applied together with known effective temperatures and metallicities

1.2.4 Miroturbulent velocity

Microturbulent velocity measures non-thermal, miniature turbulent flows in stellar atmospheres that expands spectral lines in addition it measures thermal and natural broadening processes. The spectral lines are analyzed to obtain this parameter, and neutral iron (Fe I) lines are used for this purpose. Microturbulent velocity is determined by minimizing the standard deviation of the individual Fe I lines in determining the iron abundances. This procedure removes trends between line strengths. Otherwise it would cause systematic errors. The reason to have one microturbulent velocity accurately determined is that this is necessary to build up accurate stellar atmosphere models and carry out a reliable chemical abundance analysis (Mucciarelli, 2011)

1.2.5 Metallicity

The Metallicity measures the abundance of the elements that is heavier than hydrogen in celestial stars and galaxies and so on. It is expressed as:

$$[\mathrm{Fe/H}] = \log_{10}\left(\frac{N_{\mathrm{Fe}}}{N_{\mathrm{H}}}\right) - \log_{10}\left(\frac{N_{\mathrm{Fe}}}{N_{\mathrm{H}}}\right)_\odot$$

The metallicity derived by comparing the average abundance of iron of the star with the solar reference abundance (Lindgren et al., 2016). In our work the average iron abundance which is derived by an average of a number of lines is taken as metallicity of the stellar atmosphere at the end of previous steps of the iterations.

For example, The average Fe I abundence from lines 99 and 15 was calculated as $\log_{10}\left(\frac{N_{\text{Fe}}}{N_{\text{H}}}\right) = 7.25 \pm 0.09$ dex and the solar abundance $\log_{10}\left(\frac{N_{\text{Fe}}}{N_{\text{H}}}\right)_{\odot} = 7.5$ dex, thus resulting meallicity [Fe/H] = -0.25 dex.

1.2.6 Chemical Abundance of Light Elements

Chemical abundances of light elements are used to describe the relative abundance of chemical elements on a star in a logarithmic scale with respect to hydrogen and are usually given as relative abundance with respect to the Sun. Specifically, light truths of alpha-elements like Si, Ca, also Al, Sc and Ti are major tracers of enrichment forces that are triggered by the explosion of supernova and stellar evolution. In this study, the abundances of chemicals were calculated using MOOG radiative transfer code (Sneden, 1973) (Sneden et al., 2012) with a modified linelist, where spectral lines, and atomic data were taken to the VALD database (Ryabchikova et al., 2015) The outcomes consisted of the mean abundance, standard deviation and the number of spectral lines that were used to other elements. The normalized stellar spectra were used to measure equivalent widths (EWs) of spectral lines with the ARES code in a normalized stellar spectrum of the object in question (Sousa et al., 2007) . The ARES arrangement was outlined in the mine.opt file, the important parameters were a wavelength range of 4500A to 7000A. The technique allowed abundance of light Al, Si, Ca, Sc, and Ti to be obtained and these are used to give an insight into the chemical composition and evolutionary history of the stars under study.

1.2.7 Errors of Atmospheric Parameters and Chemical Abundances

The uncertainties in the determination of the physical properties of stars is the result of spectroscopic analysis are errors of atmospheric parameters and chemical abundances. These errors are caused by a number of sources, such as, the measurement errors of the equal widths, the noise in recorded spectra, the atomic data errors, interdependencies of the atmospheric parameters. These errors should be estimated properly in order to evaluate the accuracy of the calculated stellar parameters and abundances Gray (2005).

In this study we measured uncertainties of the atmospheric parameters through spectroscopical method, that is, through the sensitivity of the derived abundances to the variation in the stellar parameters. This technique is based on the excitation equilibrium and ionization equilibrium conditions and involves typically applied processes in stellar spectroscopy procedures Sousa (2011).

The error effective temperature was determined employing the error of the slope of iron and the excitation potential. The uncertainty is related to the difference in temperature needed to cause a marked change in divorce between excitation equilibrium (Sousa et al., 2010).

The best effective temperature is one that corresponds to the case of a slope that is equal to 0. It subsequently changed the temperature until the slope was within the ranges defined by $m - \sigma_m$ and $m + \sigma_m$, where m is the fitted slope and σ_m is the uncertainty of the slope. The uncertainty is equal to

the change in temperature needed to transition from the zero-slope solution to these limiting values, representing a visible change in excitation equilibrium.
The ionization balance between Fe I and Fe II was used to determine the uncertainty in surface gravity. The value of $\log g$ was varied in the parameter space of average iron abundances ± their scatter until the difference between the mean abundances of Fe I and Fe II exceeded the acceptable limit. The uncertainty is characterized by the variation in $\log g$ required to cause a substantial difference between neutral and ionized iron abundances (Hekker et al., 2013).

The error of microturbulent velocity were calculated using the correlation between equivalent width, which was reduced and the abundance of iron. Microturbulence parameter was varied until some trend was observed in abundance verses reduced equivalent width relation (Sousa, 2011).

The microturbulent velocity was estimated by the uncertainty of the abundances of individual Fe lines, using the scatter of abundances. To begin with, the standard deviation of the Fe I abundances, σ_{line}, was determined. It was approximated to have an uncertainty of

$$\sigma \approx \frac{\sigma_{\text{line}}}{\sqrt{2(N-1)}},$$

where N is the number of Fe I lines. The velocity of the microturbulence was then adjusted till the scattering reached the limits

$$\sigma_{\text{line}} + \sigma.$$

The respective variations in v_t were considered as uncertainty of the microturbulent velocity.

1.3 Radial Velocity Determination via Cross-Correlation

In the first test, we applied the normal cross-correlation function (CCF) technique to find spectroscopic radial velocities of the target stars. The CCFs also showed a number of double-peaked profiles, which were the candidate of binary in spectroscopic double-line, and broadened profiles of fast-rotating stars. These were not included in the further analysis.

Radial velocities were determined as a result of the cross-correlation of each observed spectrum with a suitable template spectrum. The position of the maximum of the CCF was used to determine the velocity shift, and it is the best fit between the observed and template spectra (Tonry & Davis, 1979). The CCF quantifies the resemblance between the spectra, as a function of velocity shift, and is greatest at the stellar radial velocity.

The example of a well-defined CCF that has only one peak (as illustrated in Figure 4) represents a reliable radial velocity measure. Figure 5 represents a sample of fast rotating star. Figure 6, on the other hand, reveals a CCF that is doubly peaked, thus demonstrating the existence of a spectroscopic binary system. The broad and shallow CCF profiles (due to rotational line broadening) were also used to identify fast-rotating stars. In the case of these stars, radial velocity determination is less certain. Hence, binary candidates along with fast rotators were not included in the further analysis.

Cross-correlation is a tried and tested method in the spectroscopy of stars and yields a valid radial velocity in case appropriate templates are employed. More sophisticated techniques, like maximum-likelihood techniques, have also been devised to enhance the accuracy furthermore (Allende Prieto, 2007; Zucker, 2003).

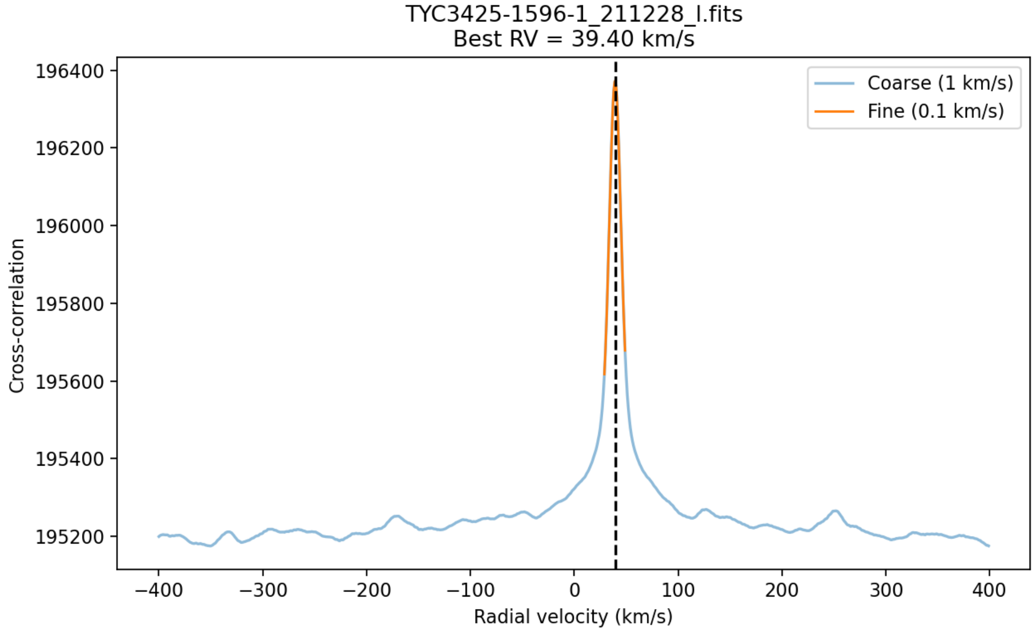

Figure 4 Cross-correlation function for the star TYC3425-1596-1. The peak corresponds to the best-fit radial velocity of 39.40 $\mathrm{km\,s^{-1}}$.

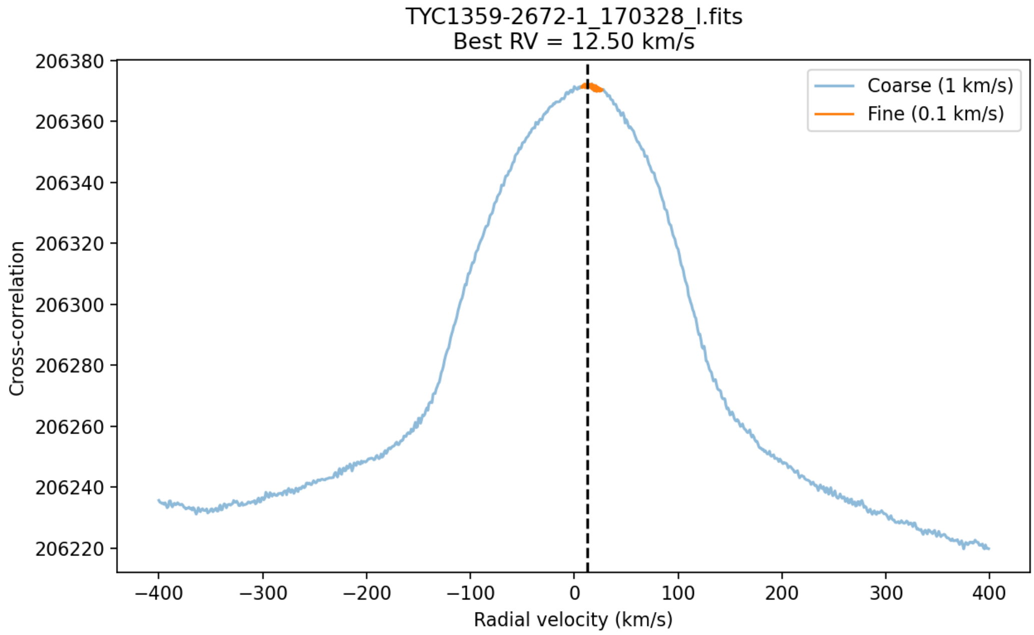

Figure 5 Cross-correlation function for the star TYC1359-2672-1.

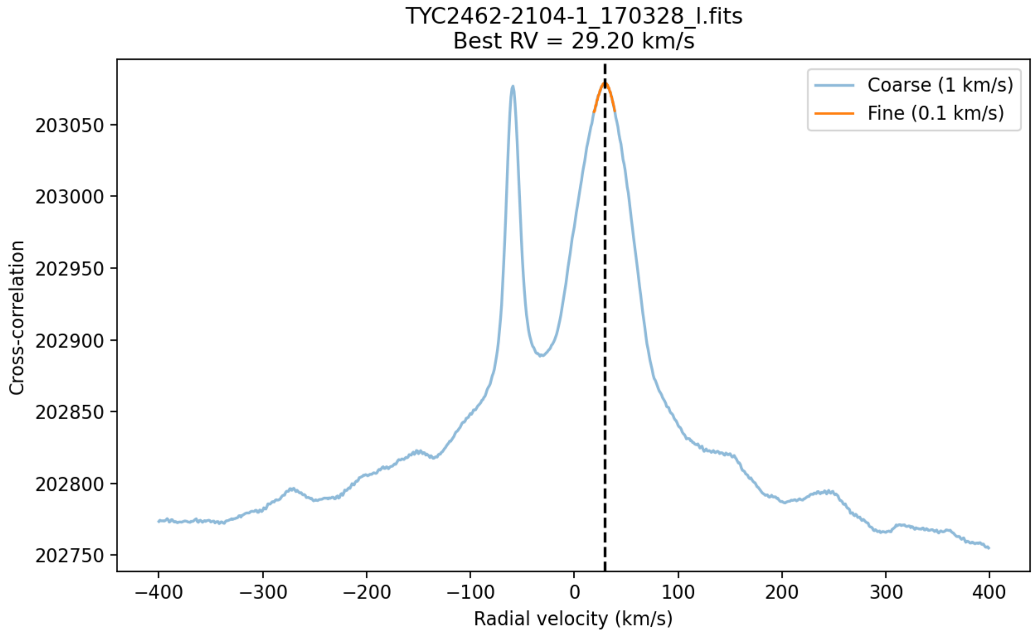

Figure 6 Cross-correlation function for the star TYC2462-2104-1. The profile shows a double-peaked structure, means the possible of a spectroscopic binary stars.

1.4 Stellar Orbital Parameters

The orbital information of the sample stars was determined using the Python package, namely, with the assistance of the program galpy which is a versatile Galactic science and orbit integration of positions (Bovy, 2015) . The current phase-space coordinates of all stars, i. e. positions, parallaxes, proper motions, and radial velocities, provided initial conditions to the calculation of the orbits. Calculation of stellar orbits was then done by disturbing equations of motion numerically in a model of an axisymmetric Galactic potential, a form of large scale representation of mass distribution of the Milky Way. One popular Milky Way potential model that was used in the work includes the contributions of the bulge, disk and dark matter halo to it (Bovy, 2015) . The key orbital parameters were obtained with the help of the resultant trajectories and included orbital eccentricity, pericentre distance and apocentre distance, mean Galactocentric radius, and the highest point of the orbit above the Galactic plane. They are parameters that are employed to provide a quantitative definition of the dynamical behaviour of stars and are needed to study both the chemo-dynamical structure of the Galaxy. Orbital model derived uncertainties are primarily escaped in terms of errors in the input astrometric and kinematic data e.g. parallaxes, proper motions, radial velocity errors etc. These sources of observations are added to the estimated orbits and merely affect the resultant orbital parameters (D’Souza & Bell, 2022) . In addition, it introduces systematic uncertainties through the assumption of things regarding the Galactic potential. Both the choice of the Milky Way model and the adopted reference frame can have a significant influence on the calculated orbital properties. Any variation in the alleged potential can translate to variation in the orbital proportions such as eccentricity, orbital radii and vertical oscillations at least the authors argue this would be the case at least we can deduce this by contrasting the theoretical models in the books and the observed on the planets of Mars and Jupiter (Beane, 2019) . Numerical errors in the integrating the orbit (e.g. what time step to take and what integration method to take) can tend to be relatively small individually, but when summed up can contribute to the total error budget. A fixed time step and tried integration functions, which are included in the computer code galpy, can be used to minimize such effects (Bovy, 2015) .

2 Results

2.1 Atmospheric Parameters and Chemical Abundances

The spectral data were measured under the high-resolution spectrograph of the telescope of the Moletai Astronomical Observatory with a diameter of 1.65 meters (VUES) (Jurgenson et al., 2016). Here we have used widths which were automatically measured using the ARES that assisted to obtain the significant parameters of lines as defined by the (Sousa et al., 2007) software. The Ares measurements were compared with the equivalent width of spectral lines of one of the stars to have a better understanding of the procedure of manual calculations and compare it to Ares measurements. This was followed by the use of stellar chemical analysis package MOOG and using the atomic parameters (Sousa et al., 2014) (Gustafsson et al., 2008).

The calculations were also automated by using custom scripts with MOOG tools and the ARES. This methodology will be discussed further below in subsections that explain how this methodology enabled us to form effective temperatures, microturbulent velocities, metallicity, and surface gravity by using separate iron lines and consequently.

The atmospheric parameters derived in this work are in good overall agreement with those reported by (Tautvaišienė et al., 2020), who analyzed 277 slowly rotating bright stars in the TESS continuous viewing zone (Tautvaišienė et al., 2020).

In our sample, the effective temperatures span from $\sim$ 4200 K to $\sim$ 6500 K, while (Tautvaišienė et al., 2020) report a broader range of 3700 K to 6600 K with a peak around 4700 K. This is likely caused by the presence of more cool giants in their sample.

We find the surface gravity ranging from $\log g \approx 1.0$ to 4.8, which includes both giants and dwarfs. Likewise, the range of $\log g$ found in the study by (Tautvaišienė et al., 2020) is between 0.8 and 3.5 for giants (peak at 2.7) and 3.6 to 4.5 for dwarfs (peak at 4.3), showing a similar mix of stellar evolutionary phases (Tautvaišienė et al., 2020)

Our sample has a narrower metallicity distribution ($[\mathrm{Fe/H}] \approx -0.65$ to +0.21) than the sample investigated by (Tautvaišienė et al., 2020) (−1.5 to +0.25 dex, peak at −0.25 dex). This implies that our sample is more centred on solar metallicity, but their sample contains more metal-poor stars.

In summary, the two works are consistent with similar ranges in the parameters, and confirm that the studied stars are mainly of the Galactic thin disk population, with a mix of dwarfs and giants. Atmospheric parameters of each star is summarized in Table 1. Evolutionary tracks of the sample stars and distribution of atmospheric parameters are described in Figure 7 and Figure 8 respectfully.

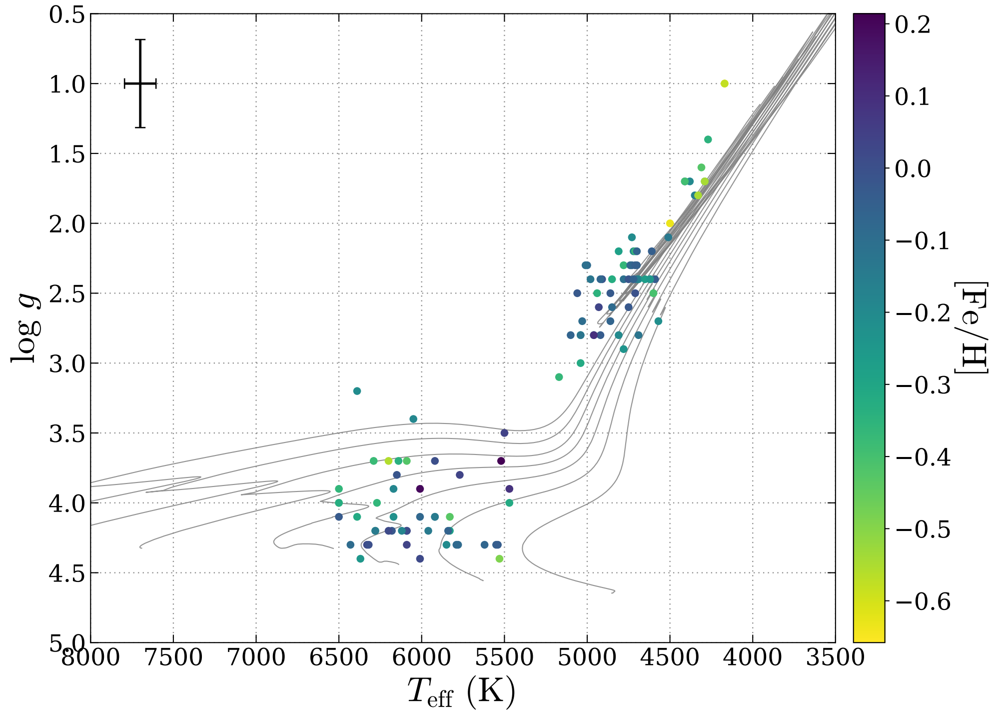

Figure 7 $\log g$ versus $T_{\rm eff}$ diagram of the investigated stars (dots) with metallicity coded by color. Evolutionary sequences from the BaSTI-IAC database for stellar masses between 0.8 and 2.0 $M_\odot$ and metallicity Z = 0.0172 are shown as gray solid lines.

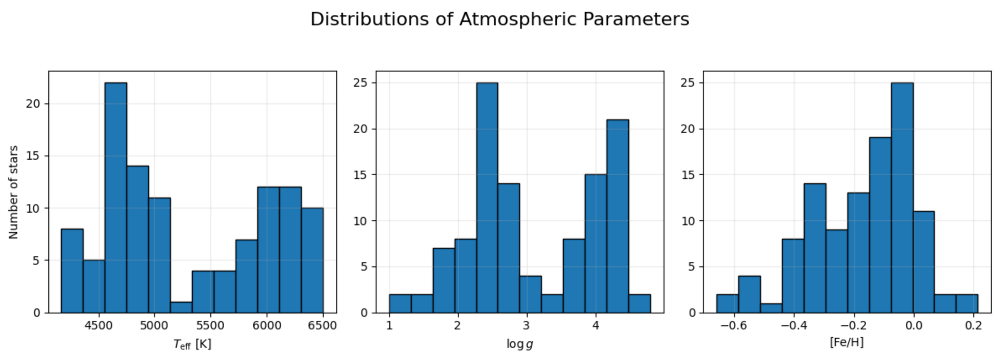

Figure 8 Distribution of atmospheric parameters

Our chemical abundance analysis is in agreement with the analysis and results of (Tautvaišienė et al., 2020), who calculated abundances for 277 bright FGK stars in the TESS continuous viewing zone.

In both cases, iron abundances are based on a large number of Fe I and Fe II lines, which guarantees reliable metallicity estimates. In our analysis we use typically 10–45 iron lines per star, similar to the line-rich analysis of (Tautvaišienė et al., 2020).

For α and iron-peak elements (Si, Ca, Ti and Cr), both analyses are based on multiple lines (typically 5-25 lines per element), leading to small line-to-line scatter and robust abundances. In particular, both analyses contain a good number of neutral lines such as Si I and Ca I, which allow for reliable abundance estimates. Average abundance of our sample stars are described in Table 2.

Elements measured from a small number of lines (Al I and Ca II) exhibit larger uncertainties in both studies. This is expected due to the large sensitivity to continuum placement, line blending and atomic data uncertainties when only a limited number of spectral lines is available.

The line-to-line scatter seen in our work is in agreement with that of (Tautvaišienė et al., 2020), where elements with many measured lines have low scatter, whereas those based on only a few lines display higher scatter. Moreover, cases for which one or more lines are missing or unusable are handled in the same way, and removed from the statistical analysis, in both studies. Number of spectral lines used for abundance determination are also described in Table 2.

In summary, the comparison between the two analyses confirms the reliability of the abundance patterns, and suggests that the chemical abundances of the studied sample follow the expected trends for Galactic disk stars.

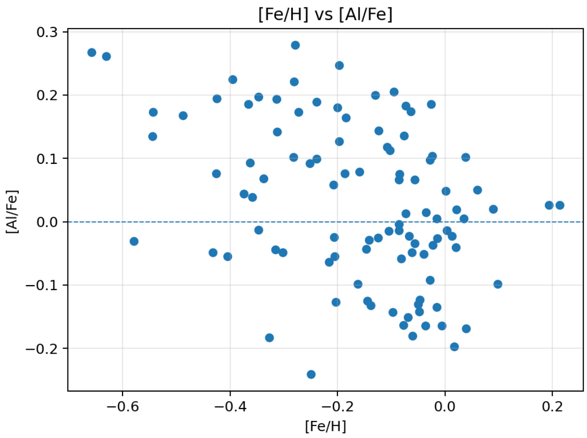

(a) [Fe/H] vs [Al/Fe]

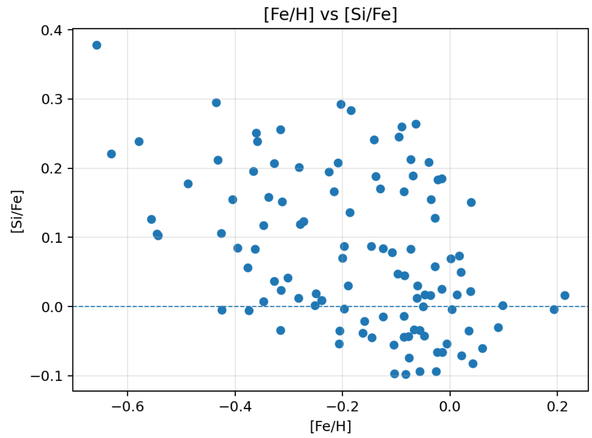

(b) [Fe/H] vs [Si/Fe]

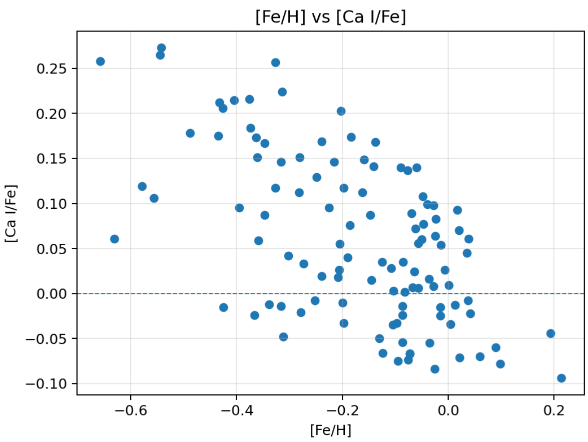

(c) [Fe/H] vs [Ca I/Fe]

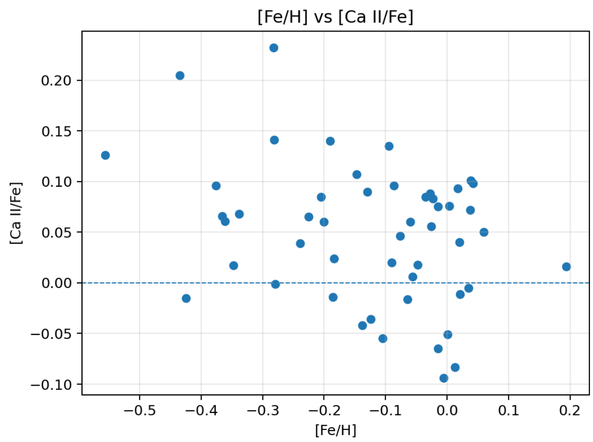

(d) [Fe/H] vs [Ca II/Fe]

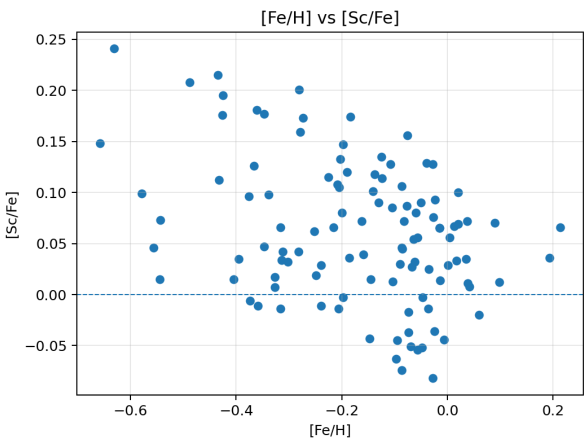

(e) [Fe/H] vs [Sc II/Fe]

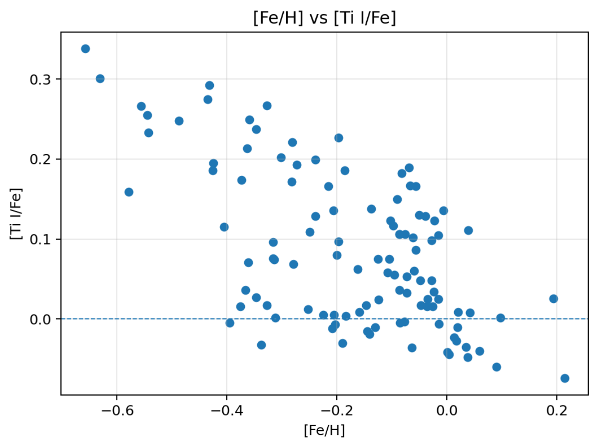

(f) [Fe/H] vs [Ti I/Fe]

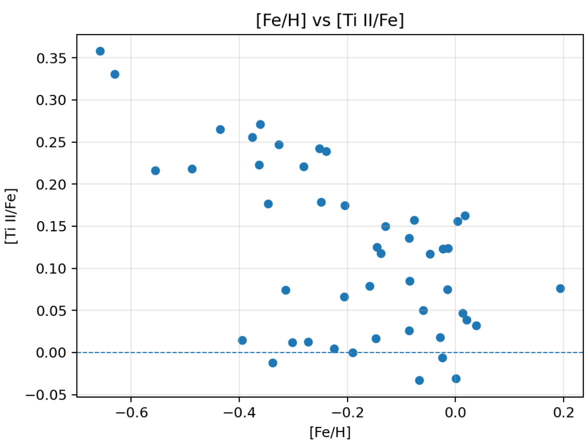

(g) [Fe/H] vs [Ti II/Fe]

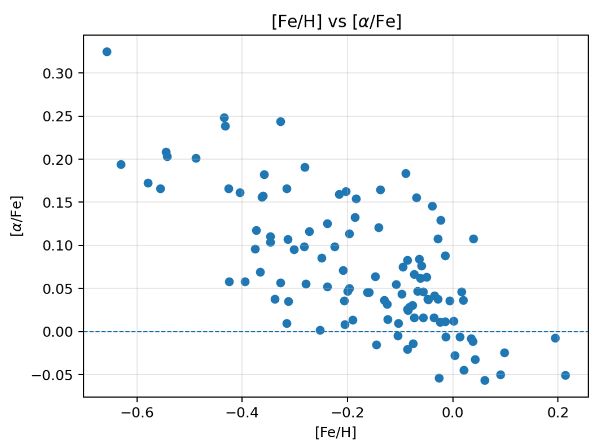

(h) [Fe/H] vs [α/Fe]

2.2 Errors on Atmospheric Parameters and Abundances

The uncertainties in the effective temperature, surface gravity, metallicity, and microturbulent velocity of each star were calculated and are given in Table 1. The typical uncertainties obtained for the full sample are approximately $\sigma_{T_{\rm eff}} \sim$ 60–120 K, $\sigma_{\log g} \sim$ 0.2–0.6 dex, $\sigma_{\rm [Fe/H]} \sim$ 0.10–0.20 dex, and $\sigma_{\xi} \sim$ 0.2–0.7 km s^{-1}. There are few stars which have larger uncertainties, and these are probably those which have lower signal-to-noise spectra or less reliable spectral fits. These stars lead to the overall scatter in the derived relations but do not substantially impact the overall trends in this study.

Generally, the estimated uncertainties suggest that the atmospheric parameters are fairly well constrained throughout much of the sample and are comparable to those generally obtained in spectroscopic analyses of Galactic field stars.

2.3 Distributions of Orbital Parameters

In this study observational data was transformed into Galactocentric reference frame on standard conventions. Solar system SOLAR model SOLAR calculates Stellar orbits using the Python software package, galpy, a numerical integrator of the equations of motion in an axisymmetric Galactic potential which is an approximation of the mass distribution of the Milky Way at large scale. Initial conditions applied in the orbit computations presumably relying on the astrometric positions, parallaxes, proper motions, and radial velocities of the two stars were the current phase-space coordinates of the two stars. These values were converted to a Galactocentric coordinate system which is compatible with the conventions used in the GALPY software. A large-scale gravitational field of the Milky Way was assumed to be axisymmetric when represented in Galactic potential. A fixed time step was fixed to numerically integrate the equations of motion with the aim of checking the numerical stability of the system. Depending on the obtained orbits, valuable orbital parameters like eccentricity, pericentre and apocentre distance, mean Galactocentric radius and height to maximum value above the Galactic plane were derived. The parameters provide a quantitative expression of the orbital properties of stars and make a basis of the chemo-dynamical study of the sample.

By integrating the trajectories of the new Tycho-2 sources, we derived Galactic orbital parameters of the new sources using an axisymmetric Milky Way potential (e.g., with `galpy` e.g. `MWPotential2014`). To compute these summary quantities each star was integrated over a multi-Gyr time interval using a uniform time grid and then we computed the summary quantities that characterise the radial and vertical excursions.

Standard orbital eccentricity, e, was computed based on the integrated orbit using the standard definition of galpy. The minimum and maximum of the Galactocentric cylindrical radii reached during the integration, i.e. $R_{\rm min}$ and $R_{\rm max}$, were obtained. The vertical motion was measured by the extremes of the vertical coordinate, $Z_{\rm min}$ and $Z_{\rm max}$ which were calculated along the combined orbit, and the maximum absolute vertical amplitude was determined as.

$$|Z|_{\rm max} \equiv \max\left(|Z|\right), \tag{1}$$

in line with the output of the galpy command, i.e. zmax( ). Lastly, the mean Galactocentric radius of the orbit, was calculated as the time-average of R(t) / r (t) along the orbit,

$$\langle R \rangle = \frac{1}{N} \sum_{i=1}^{N} R(t_i), \tag{2}$$

with t i being the time samples of integration.

The resulting parameters Table 3 cover a range of orbital shapes, between nearly circular disk-like orbits with very low eccentricity (e.g., $e \sim 0.01$) and more stretched out trajectories with $e \gtrsim$ 0.30 -0.40 and much higher apocentric radii. Most objects are still trapped near the Galactic plane with small vertical amplitudes and a few of them have large vertical amplitudes (up to several kpc) indicating populations that are kinemically hotter. Repeated records with the same Tycho-2 ID but differing suffixes are associated with repeated observations/solutions and thus they give the same orbital parameters.

Besides computing the classical orbital parameters, we have also computed the orbital actions and angular momentum of all the stars in the sample. Our results are tabulated in Table 3 where we report the angular momentum of the orbit about the z-axis, L z, the radial action J R, the vertical action J z, the guiding-centre radius R g, and the orbital eccentricity e.

2.4 Spatial Distribution of Chemical Abundances in Galactic disk

We analyzed the spatial distribution of metallicity by multiplying the chemical abundances of the sample stars with the orbital parameters of the sample stars. To trace the radial and vertical structure of the disk, the mean Galactocentric radius, the mean of the radial and vertical excursions, was used and the value of this quantity was determined: the mean Galactocentric radius, and the maximum vertical excursion.

A weak negative trend of [Fe/H] with [R] is observed which decreases in the inner regions to [Fe/H] = -0.3 dex at larger radii equivalent to a gradient of = -0.03 to = -0.05 dex/kpc. There also exists a noticeable dispersion of the order of 0.1-0.2 dex at all radii which is probably a reflection of the effects of radial migration.

Stars with lower values of [Fe/H] are generally more metal-rich ([Fe/H] $\gtrsim -0.1$) and those with higher values of [Fe/H] exhibit lower values of [Fe/H]. This behaviour is in line with the shift between the thin disk to a population of thick disk at a higher degree of kinematic heat.

The overall results suggest that the sample contains both dynamically cold, metal-rich thin disk stars and more extended, metal-poor, thick disk candidates, as it would be expected of the standard chemo-dynamical structure of the Galactic disk.

2.5 Radial and vertical orbital diagnostics

Figure 10 shows the present-day Galactocentric radius (R_{current}), the time-averaged guiding radius (R_{mean}), the present-day height above the Galactic plane (Z_{current}), and the maximum vertical excursion ($|Z_{\text{max}}|$) as a function of star index for the full sample. The distribution of R_{current} is tightly clustered around the Solar circle, remaining close to ~ 8 kpc for nearly all objects, with only a small number of stars reaching slightly larger radii ($\lesssim$ 8.7 kpc). In contrast, R_{mean} spans a much broader range (from ~ 6.5 to ~ 14.1 kpc), demonstrating that while the stars are observed near the Solar neighborhood, their orbits probe substantially different mean radii. This behavior is consistent with a mixture of nearly circular thin-disk orbits and more eccentric trajectories that carry stars inward and outward relative to the Solar radius.

The vertical coordinates show a similarly layered structure. The instantaneous heights are generally small, with Z_{current} typically $\lesssim$ 0.35 kpc, indicating that most targets are currently close to the Galactic mid-plane. However, the maximum vertical amplitudes exhibit a wide dispersion: the majority of stars have modest excursions ($|Z_{\text{max}}|$ of order $\lesssim$ a few kpc), while a small subset reaches very large values (up to ~ 37 kpc). These high-$|Z_{\text{max}}|$ outliers indicate stars on strongly vertically extended orbits, consistent with a dynamically hotter component (e.g. thick disk/halo interlopers) within an otherwise predominantly disk-like sample. Overall, the figure highlights that the sample is kinematically heterogeneous: stars share a common present-day location near the Solar circle, but differ markedly in their characteristic radial and vertical orbital extents. Resent day Galactic positions of the analysed stars are described in Table 4

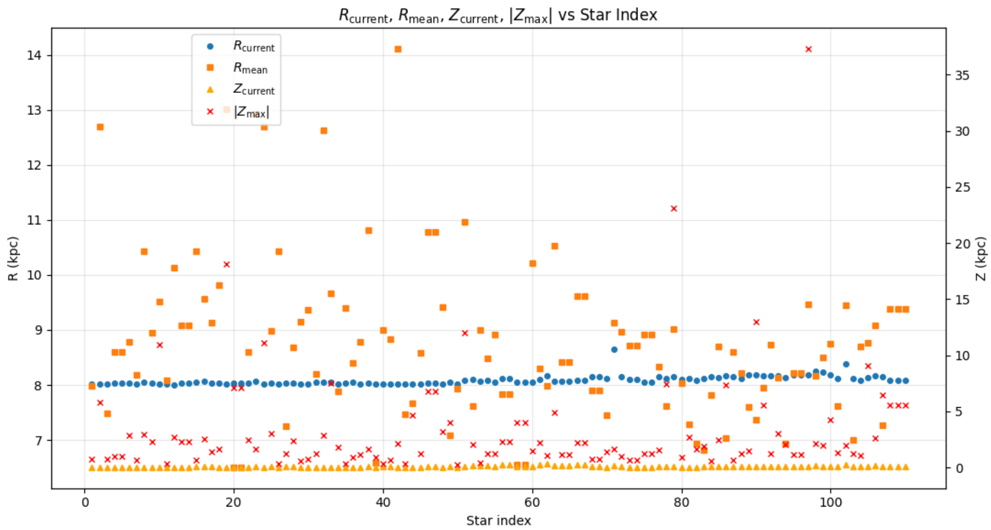

Figure 10 Vertical and radial positions of the sample stars

Figure 11 shows the orbit of a representative star from the sample projected onto the meridional (R–Z) plane. The trajectory was obtained by numerically integrating the equations of motion in the adopted axisymmetric Galactic potential using the present-day phase-space coordinates as initial conditions.

The orbit exhibits regular, quasi-periodic motion, with the star oscillating radially between approximately $R \simeq 6.0$ and 8.4 kpc while remaining vertically confined within $|Z| \lesssim 0.3$ kpc. The symmetric pattern with respect to the Galactic mid-plane indicates a dynamically cold orbit, characteristic of disk stars. The repeated crossing of the mid-plane and the absence of strong vertical excursions further suggest that this object belongs to the thin-disk population.

The box-like shape of the trajectory in the R–Z projection reflects the superposition of radial epicyclic motion and vertical oscillations, as expected for stars on nearly planar orbits in an axisymmetric potential. This example illustrates the typical orbital behavior observed for a large fraction of the sample, which is dominated by stars with small vertical amplitudes and moderate radial excursions around the Solar circle.

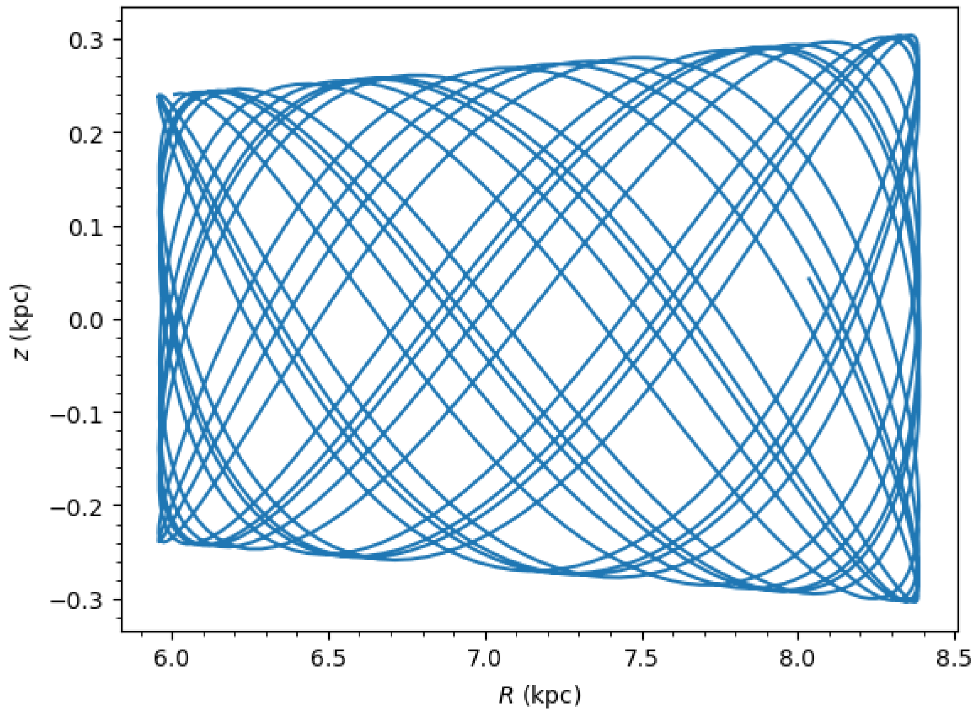

Figure 11 Meridional (R–Z) projection of the orbit.

2.6 Radial Orbital Properties and Metallicity Dependence

Figure 12 shows the relation between stellar metallicity, [Fe/H], and the maximum vertical excursion from the Galactic plane, $Z_{\max}$, for the full sample of 110 stars Most stars are trapped in low vertical heights and have near-solar to moderately sub-solar metallicities of the stars, which are in agreement with the dominant thin-disc population.

There is a negative correlation between [Fe/H] and $Z_{\max}$. A linear least-squares fit yields a vertical metallicity gradient of

$$\frac{d[\mathrm{Fe/H}]}{dZ_{\max}} = -0.095 \pm 0.027\ \mathrm{dex\ kpc^{-1}}.$$

This implies that the stars that are far away, in relation to the Galactic plane, are on average more metal-poor. The derived gradient is however affected by a relatively small number of stars with large vertical excursions that have very low metallicities than the bulk of the sample.

The gradient measured is generally consistent with the earlier research of the Galactic disc. In one example, when stellar populations are segregated in terms of their own alpha-abundance (a proxy of age), the vertical metallicity gradient of individual populations is found to be weak or nearly flat, which indicates that the global gradient observed in mixed samples is due in large part to population superposition rather than to an underlying continuous intrinsic trend. Equally, the mono-age stellar populations in the study of Xiang et al. (2015) have found that the different vertical gradients of the mono-age stellar populations have different values, with the older populations having increasingly negative values.

The negative gradient obtained in this study is perhaps indicative of the replacement of a chemically enriched thin disc, by a more metal-poor thick-disc population at higher and higher vertical heights. This is further supported by the fact that the scatter at low $Zmax$ is quite substantial, and this also implies that the stars with a wide range of chemical abundances but similar orbital confinement can be found. This behaviour is typically explained by the radial migration and the fact that different populations of the Galaxies overlap with each other Anders et al. (2017).

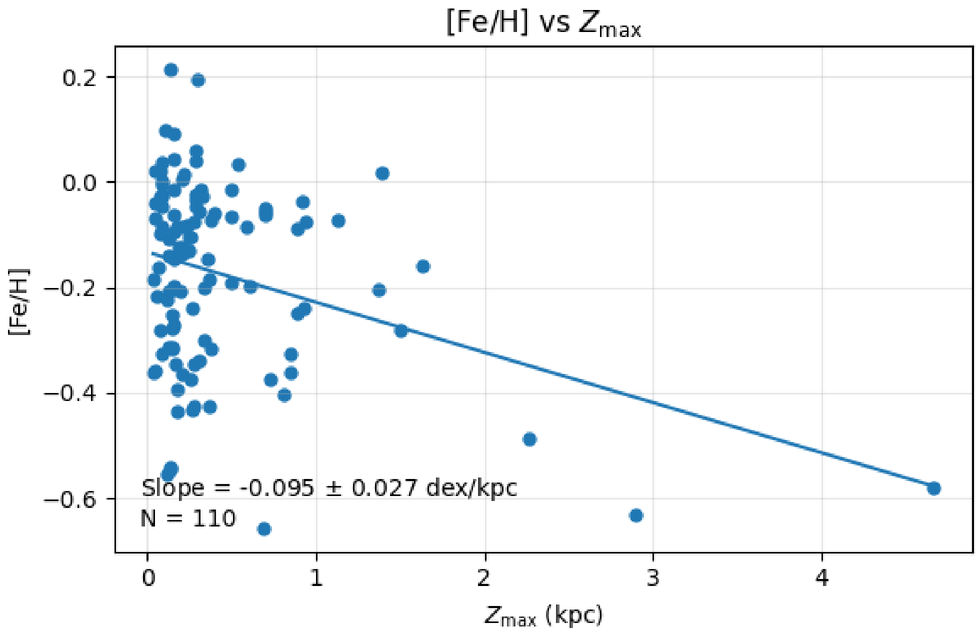

Figure 12 Vertical metallicity gradient of the sample stars.

Figure 13 indicates the correlation between stellar metallicity and the mean Galactocentric radius, R_{mean}, for the full sample stars. The stars have a radial range of about 6 to 14 kpc, with the majority lying in the range of 7 to 10 kpc. There is a weak negative trend, with a linear fit yielding a radial metallicity gradient of

$$\frac{d[\text{Fe/H}]}{dR_{\text{mean}}} = -0.015 \pm 0.012 \text{ dex kpc}^{-1}.$$

With the relatively high uncertainty, this gradient is statistically marginal and is consistent with a near-flat radial metallicity distribution. This value is much shallower than the canonical radial metallicity gradients measured for thin-disc stars (typically of the order of -0.05 dex kpc^{-1}; Boeche et al. 2013), but is consistent with studies that find the radial metallicity gradient decreases progressively with both vertical height and stellar age (Anders et al., 2017; Hayden et al., 2014).

Flattening that is evident in the current work may be explained by a number of factors. First, the application of the use of the mean orbital radius of stars, as opposed to the birth radius of the star, naturally lowers the observed gradient. Second, stars of various Galactic populations, with a wide range of vertical heights and ages, result in a significant mixing of chemical properties. The observed radial metallicity gradient can be significantly flattened by such population mixing and radial migration as demonstrated by the works of Schlesinger & et al. (2014) and Anders et al. (2017).

The big scatter in [Fe/H] at a given R mean also reflects the heterogeneous nature of the sample, and the effects of radial migration, which redistributes stars of different birth radii across the Galactic disc. Thus, the almost flat radial gradient we have derived here is probably not a reflection of the intrinsic chemical structure of the thin disc, but a combination of the effects of orbital mixing and population overlap.

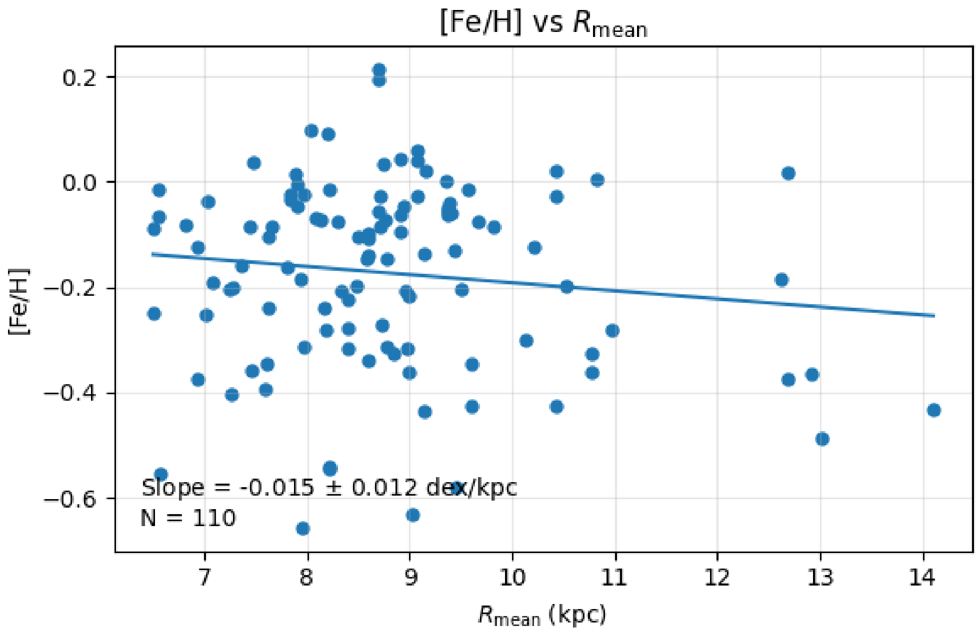

Figure 13 Radial metallicity gradient of the stellar sample.

3 Summary and Conclusions

In our study, a combined spectroscopic-dynamical study of a sample of 110 stars in the Solar neighbourhood is presented. The main atmospheric parameters, such as effective temperature, ($T_{\rm eff}$), surface gravity, (log g), metalicity, ([Fe/H]) and microturbulent velocity, along with chemical abundances of selected alpha-elements were determined using high-resolution spectra obtained using the Vilnius University Echelle Spectrograph. Moreover, astrometric and kinematic data were used to determine Galactic orbital parameters and explore the chemo-dynamical properties of the sample.

The derived atmospheric parameters span a range of $T_{\rm eff} \sim 4840$–6280 K, $\log g \sim 2.4$–4.4, and metallicities between $-0.44 \leq$ [Fe/H] $\leq +0.03$. The values suggest that there are dwarf and giant stars in the sample that represent various evolutionary phases. The abundance patterns of the alpha-elements are consistent with those predicted of Galactic disk stars, and are in good agreement with previous spectroscopic observations of similar stellar samples.

The stellar orbits were computed using the galpy package in an axisymmetric Galactocentric potential which allowed us to derive orbital parameters like eccentricity, pericentric and apocentric distance, mean Galactocentric radius ($R_{\rm mean}$) and maximum vertical excursion ($Z_{\rm max}$). Most stars are dynamically cold or slightly heated, with low eccentricities and small vertical amplitudes, whereas some smaller fraction of stars is found to have kinemical properties indicative of the thick disk populations.

We examined the dependence between metallicity and orbital elements and composed a vertical metallicity gradient of.

$$\frac{d[\mathrm{Fe/H}]}{dZ_{\rm max}} = -0.095 \pm 0.027 \text{ dex kpc}^{-1},$$

which implies that stars that become more distant to the Galactic plane are more generally more metal-poor. This trend represents the shift of the chemically enriched thin disk population to the more metal-poor thick disk population. Radial metallicity gradient, in contrast, is given as,

$$\frac{d[\mathrm{Fe/H}]}{dR_{\rm mean}} = -0.015 \pm 0.012 \text{ dex kpc}^{-1},$$

is superficial and statistically insignificant, indicating almost a flat radial metallicity distribution in the sampled range. This flattening is presumably due to the radial migration and mixing of the populations of stars of different ages and orbits.

The chemical and dynamical analysis combined proves that most of the sample stars are in the Galactic thin disk, with the smaller contribution made by the thicker disk populations. The observed scatter in metallicity at fixed orbital parameters points to the complex interplay of stellar migration, population overlap and the processes of Galactic evolution.

This study shows the significance of integrating high-resolution spectroscopy examination with orbital data to study the chemo-dynamical organization of the Milky Way. By extending these studies to larger samples, as well as introducing more detailed models of Galactic potentials, we will be able to gain even deeper insights into the processes of formation and evolution of Galactic stellar populations.

References

Allende Prieto, C. 2007, arXiv e-prints [0707.2764]

Anders, F., Chiappini, C., Minchev, I., & et al. 2017, Astronomy & Astrophysics, 600, A70

Anders, F., Chiappini, C., & Santiago, B. X. e. a. 2014, Astronomy & Astrophysics, 564, A115

Beane, A. e. a. 2019, arXiv e-prints [1905.08803]

Bensby, T., Feltzing, S., & Oey, M. S. 2014, A&A, 562, 28

Boeche, C., Siebert, A., & Piffl, T. e. a. 2013, Astronomy & Astrophysics, 559, A59

Bovy, J. 2015, The Astrophysical Journal Supplement Series, 216, 29

Chiappini, C., Matteucci, F., & Gratton, R. 1997, The Astrophysical Journal, 477, 765

D'Souza, R. & Bell, E. F. 2022, Monthly Notices of the Royal Astronomical Society, 512, 739

Gray, D. F. 2005, The Observation and Analysis of Stellar Photospheres (Cambridge University Press)

Gustafsson, B., Edvardsson, B., Eriksson, K., et al. 2008, A&A, 486, 951

Hayden, M. R., Bovy, J., Holtzman, J. A., & et al. 2014, The Astronomical Journal, 147, 116

Hekker, S., Elsworth, Y., Mosser, B., et al. 2013, Astronomy Astrophysics, 556, A59

Jurgenson, C., Fischer, D., McCracken, T., et al. 2016, Journal of Astronomical Instrumentation, 5, 1650003

Lindgren, S., Heiter, U., & Seifahrt, A. 2016, Astronomy Astrophysics, 586, A100, published online: 02 February 2016

Mikolaitis, , Tautvaišienė, G., Drazdauskas, A., et al. 2018, Publications of the Astronomical Society of the Pacific, 130, 074202

Mucciarelli, A. 2011, Astronomy Astrophysics, 528, A44, published online: 28 February 2011

Ryabchikova, T., Piskunov, N., Kurucz, R. L., et al. 2015, Phys. Scr, 90, 054005

Schlesinger, K. J. & et al. 2014, The Astrophysical Journal, 791, 112

Sneden, C. 1973, ApJ, 184, 839

Sneden, C., Bean, J., Ivans, I., Lucatello, S., & Sobeck, J. 2012, MOOG: LTE line analysis and spectrum synthesis, Astrophysics Source Code Library, record ascl:1202.009

Sousa, S. G., Alapini, A., Israelian, G., & Santos, N. C. 2010, Astronomy Astrophysics, 512, A13

Sousa, S. G., Santos, N. C., Adibekyan, V., et al. 2014, A&A, 561, A21

Sousa, S. G., Santos, N. C., Israelian, G., Mayor, M., & Monteiro, M. J. P. F. G. 2007, A&A, 469, 783

Sousa, S. G. e. a. 2011, AA, 533, A141

Tautvaišienė, G., Mikolaitis, Š., et al. 2020, ApJS

Tonry, J. & Davis, M. 1979, Astronomical Journal, 84, 1511

Škoda, P., Draper, P. W., Neves, M. C., Andrešič, D., & Jenness, T. 2014, Astronomy and Computing, 7, 108

Xiang, M. S., Liu, X. W., Yuan, H. B., & et al. 2015, Research in Astronomy and Astrophysics, 15, 1209

Zucker, S. 2003, Monthly Notices of the Royal Astronomical Society, 342, 1291

A Appendix

Table 1 Atmospheric parameters of the investigated stars.

Tycho-2 ID	$T_{\rm eff}$ (K)	$\Delta T_{\rm eff}$ (K)	$\log g$ (dex)	$\Delta \log g$ (dex)	[Fe/H] (dex)	Δ[Fe/H] (dex)	v_t (km s^{-1})	Δv_t (km s^{-1})
TYC1381-1638-1	6180	10	4.20	0.35	-0.02	0.15	1.90	0.47
TYC1383-84-1	6290	14	3.70	0.45	-0.38	0.17	1.90	0.55
TYC1388-1791-1	5770	14	3.80	0.24	0.04	0.11	1.30	0.23
TYC1894-1961-1	5920	81	4.10	0.32	-0.11	0.14	1.00	0.50
TYC1894-1961-1	5960	85	4.20	0.29	-0.14	0.13	0.90	0.47
TYC1898-2479-1	5830	78	4.20	0.13	-0.28	0.12	1.00	0.40
TYC1898-787-1	5920	56	4.10	0.21	-0.15	0.09	1.20	0.40
TYC1899-1584-1	6090	89	3.70	0.33	-0.42	0.13	1.30	0.44
TYC1900-1598-1	5550	79	4.30	0.17	-0.05	0.14	1.20	0.43
TYC1907-321-1	5850	79	4.30	0.23	-0.20	0.10	1.10	0.37
TYC1933-747-1	5620	86	4.30	0.18	-0.07	0.16	0.90	0.71
TYC1936-1174-1	6280	94	4.20	0.29	-0.30	0.11	1.10	0.40
TYC1942-1827-1	6090	106	4.30	0.37	0.04	0.16	1.30	0.50
TYC1942-1827-1	6090	80	4.20	0.28	0.06	0.12	1.30	0.40
TYC1951-1481-1	6500	107	4.10	0.35	-0.03	0.12	1.20	0.35
TYC1952-1819-1	6150	134	3.80	0.50	-0.02	0.20	1.20	0.65
TYC1954-529-1	6500	159	4.00	0.41	-0.44	0.15	2.40	0.94
TYC2455-727-1	5780	62	4.30	0.22	-0.09	0.10	1.00	0.37
TYC2473-1324-1	5530	72	4.40	0.27	-0.49	0.13	0.90	0.10
TYC2477-541-1	6430	330	4.80	1.02	-0.09	0.40	2.50	2.10
TYC2477-541-1	6370	200	4.50	0.57	-0.25	0.23	1.80	1.05
TYC2485-2097-1	6140	155	3.70	0.60	-0.34	0.23	2.40	0.85
TYC2488-121-1	5170	79	3.10	0.10	-0.37	0.17	1.00	0.50
TYC2488-849-1	6200	107	4.20	0.36	0.02	0.15	1.50	0.50
TYC2490-1679-1	6390	348	4.10	0.97	-0.32	0.36	2.50	0.77
TYC2495-846-1	6010	74	4.40	0.24	0.02	0.11	1.00	0.35
TYC2500-1087-1	6390	170	3.20	0.54	-0.20	0.20	1.70	0.57
TYC2507-1255-1	6320	76	4.30	0.13	0.00	0.12	1.60	0.27
TYC2507-809-1	6010	112	3.90	1.40	0.19	0.13	1.20	0.69
TYC2507-947-1	6330	138	4.30	0.19	0.02	0.18	0.90	0.61
TYC2927-323-1	5470	80	3.90	0.31	0.09	0.15	0.90	0.70
TYC2948-322-1	6170	86	3.90	1.12	-0.19	0.11	1.40	0.50
TYC2952-543-1	6010	76	4.10	0.22	-0.08	0.12	1.30	0.34
TYC2953-1958-1	6090	75	4.20	0.13	0.01	0.10	1.30	0.20
TYC2957-1441-1	5540	62	4.30	0.22	-0.04	0.11	1.00	0.40
TYC2958-1173-1	6170	160	4.10	0.53	-0.22	0.22	2.40	1.20
TYC2961-1900-1	5470	67	4.00	0.26	-0.31	0.12	0.90	0.42
TYC2973-423-1	5920	79	3.70	0.30	0.00	0.12	1.10	0.28
TYC2984-1187-1	6200	125	3.70	0.40	-0.56	0.15	1.20	0.68
TYC2991-699-1	6500	114	3.90	0.42	-0.36	0.15	1.90	0.83
TYC2991-699-2	6500	109	4.00	0.39	-0.33	0.14	1.60	0.78
TYC3396-2196-1	5830	66	4.10	0.32	-0.43	0.11	1.10	0.40
TYC3401-1647-1	6270	77	4.00	0.14	-0.36	0.11	1.40	0.20
TYC3415-2484-1	5790	52	4.30	0.19	-0.08	0.10	1.10	0.40
TYC3423-573-1	6280	132	4.20	0.42	-0.14	0.16	1.00	0.65
TYC3425-1596-1	4780	42	2.30	0.50	-0.36	0.12	1.50	0.16
TYC3425-1596-1	4850	51	2.40	0.44	-0.33	0.18	1.40	0.24
TYC3427-1400-1	5840	74	4.20	0.26	-0.06	0.12	0.90	0.58
TYC3796-306-1	6050	122	3.40	0.43	-0.19	1.17	1.80	0.45
TYC3797-247-1	6120	96	4.20	1.35	-0.18	0.13	0.90	0.77
TYC4133-206-1	4810	87	2.20	1.30	-0.28	0.11	1.40	0.14
TYC4133-256-1	4780	101	2.40	0.45	-0.10	0.19	1.30	0.41
TYC4142-1234-1	4570	95	2.70	0.55	-0.22	0.20	2.50	0.55
TYC4143-1061-1	4720	93	2.20	0.57	-0.20	0.20	1.40	0.35

Tycho-2 ID	T_{eff} (K)	ΔT_{eff} (K)	$\log g$ (dex)	$\Delta \log g$ (dex)	[Fe/H] (dex)	Δ[Fe/H] (dex)	v_t (km s^{-1})	Δv_t (km s^{-1})
TYC4152-127-1	5030	90	2.70	0.50	-0.10	0.17	1.40	0.45
TYC4152-1342-1	4750	108	2.40	0.59	-0.02	0.18	1.30	0.59
TYC4152-1342-1	4860	96	2.70	0.54	-0.07	0.16	1.50	0.48
TYC4152-569-1	4920	98	2.80	0.60	-0.04	0.16	2.50	0.46
TYC4152-569-1	4750	95	2.60	0.55	-0.02	0.15	1.70	0.47
TYC4159-1214-1	4620	90	2.40	0.51	-0.08	0.15	1.50	0.51
TYC4159-1294-1	4290	97	1.70	0.62	-0.31	0.16	1.90	0.50
TYC4159-1359-1	4380	116	1.70	0.78	-0.20	0.22	1.60	0.61
TYC4159-454-1	4690	119	2.80	0.80	-0.12	0.19	1.90	0.55
TYC4160-223-1	4960	92	2.80	0.44	-0.28	0.16	0.90	0.41
TYC4160-223-1	5040	96	3.00	0.48	-0.32	0.18	0.90	0.45
TYC4168-694-1	4270	125	1.40	0.90	-0.35	0.23	1.90	0.61
TYC4168-694-1	4310	115	1.60	0.86	-0.43	0.25	1.70	0.65
TYC4305-1262-1	4610	95	2.20	0.55	-0.05	0.15	1.50	0.50
TYC4305-1262-1	4710	79	2.50	0.50	-0.01	0.14	1.50	0.48
TYC4306-315-1	4850	90	2.60	0.50	-0.09	0.14	1.30	0.45
TYC4308-248-1	4510	105	2.10	0.65	-0.14	0.17	2.40	0.60
TYC4309-1078-1	5040	90	2.80	0.50	-0.21	0.15	0.90	0.45
TYC4318-2488-1	5060	88	2.50	0.54	-0.03	0.15	1.70	0.49
TYC4318-2488-1	5000	78	2.30	0.55	-0.09	0.16	1.50	0.51
TYC4320-2109-1	5500	110	3.50	0.70	0.04	0.18	2.50	0.54
TYC4320-2109-1	5100	89	2.80	0.60	-0.06	0.16	1.30	0.45
TYC4321-805-1	4730	105	2.10	0.65	-0.21	0.17	1.00	0.44
TYC4321-839-1	4690	100	2.40	0.60	-0.24	0.17	1.40	0.50
TYC4322-1310-1	4500	135	2.00	1.00	-0.63	0.30	1.40	0.68
TYC4322-2075-1	4960	95	2.80	0.50	0.10	0.16	1.40	0.39
TYC4323-1742-1	5040	90	2.80	0.52	-0.12	0.16	1.20	0.42
TYC4323-618-1	4810	89	2.80	0.50	-0.20	0.16	0.90	0.40
TYC4325-1243-1	4740	78	2.30	0.37	-0.08	0.15	1.30	0.42
TYC4325-1563-1	4700	98	2.40	0.55	-0.16	0.16	1.60	0.43
TYC4333-423-1	4700	90	2.30	0.50	-0.06	0.14	1.40	0.35
TYC4335-1122-1	4590	95	2.40	0.49	-0.04	0.14	1.90	0.55
TYC4335-2103-1	4410	118	1.70	0.75	-0.10	0.17	1.60	0.60
TYC4335-2105-1	4910	89	2.40	0.47	-0.01	0.14	1.20	0.45
TYC4336-886-1	4410	113	1.70	0.58	-0.40	0.22	1.70	0.33
TYC4338-1941-1	4170	112	1.00	0.66	-0.66	0.19	2.00	0.31
TYC4338-1942-1	4650	157	2.40	1.04	-0.27	0.35	1.60	0.71
TYC4338-647-1	4350	103	1.80	0.65	-0.16	0.18	1.40	0.49
TYC4339-2106-1	4920	95	2.40	0.50	-0.07	0.14	1.30	0.45
TYC4339-2273-1	4710	112	2.20	0.63	-0.37	0.22	1.20	0.38
TYC4339-2274-1	4290	144	1.70	1.10	-0.54	0.34	1.90	0.67
TYC4339-2274-1	4330	140	1.80	1.00	-0.55	0.31	1.70	0.70
TYC4341-343-1	4170	152	1.00	1.12	-0.58	0.32	1.10	0.71
TYC4341-936-1	4780	97	2.90	0.38	-0.24	0.17	2.10	0.39
TYC4346-356-1	5010	96	2.30	0.55	-0.10	0.15	1.70	0.29
TYC4347-1476-1	4930	89	2.60	0.50	0.04	0.15	1.40	0.31
TYC4348-745-1	4940	110	2.50	0.61	-0.35	0.18	1.50	0.50
TYC4350-447-1	4980	95	2.40	0.53	-0.13	0.15	1.10	0.28
TYC4351-949-1	4620	100	2.40	0.58	-0.25	0.18	1.50	0.30
TYC4351-979-1	5520	82	3.70	0.33	0.21	0.13	1.50	0.42
TYC4352-264-1	4730	95	2.30	0.55	-0.07	0.15	1.00	0.45
TYC4353-91-1	4860	110	2.50	0.65	-0.03	0.16	2.50	0.56
TYC4354-698-1	4600	110	2.50	0.70	-0.40	0.20	2.50	0.59
TYC4361-1793-1	4720	95	2.40	0.57	-0.06	0.15	1.50	0.39
TYC4361-1793-1	4710	83	2.30	0.55	-0.05	0.15	1.50	0.35
TYC4361-1793-1	4700	81	2.20	0.55	-0.06	0.15	1.50	0.35

Table 2 Absolute abundances, standard deviations, and number of lines used for the investigated stars.

Tycho-2 ID	Al I			Si I			Ca I			Ca II			Sc II			Ti I			Ti II		
	A(Al I)	σ	N	A(Si I)	σ	N	A(Ca I)	σ	N	A(Ca II)	σ	N	A(Sc II)	σ	N	A(Ti I)	σ	N	A(Ti II)	σ	N
TYC1381-1638-1	6.39	0.08	2	7.67	0.09	12	6.40	0.08	8	6.40	0.03	2	3.22	0.18	11	5.05	0.17	32	5.05	0.19	6
TYC1383-84-1		0.00	1	7.19	0.18	11	6.18	0.15	7	6.06	0.05	2	2.87	0.18	10	4.59	0.14	17	4.83	0.15	6
TYC1388-1791-1	6.59	0.04	2	7.57	0.13	12	6.37	0.07	8	6.45	0.27	2	3.26	0.23	11	4.94	0.14	32	5.02	0.19	6
TYC1894-1961-1	6.46	0.08	2	7.48	0.13	12	6.26	0.15	8		0.00	1	3.17	0.19	11	4.90	0.16	32		0.00	6
TYC1894-1961-1	6.28	0.12	2	7.61	0.13	12	6.34	0.12	8		0.00	2	3.11	0.20	11	4.79	0.21	32		0.00	6
TYC1898-2479-1	6.39	0.04	2	7.43	0.12	12	6.21	0.06	8	6.20	0.26	2	3.07	0.12	11	4.89	0.15	32	4.89	0.20	6
TYC1898-787-1	6.26	0.19	2	7.45	0.10	12	6.28	0.11	8	6.30	0.25	2	2.96	0.18	11	4.82	0.13	32	4.82	0.08	6
TYC1899-1584-1	6.22	0.15	2	7.08	0.08	12	5.90	0.08	8	5.90	0.01	2	2.92	0.11	11	4.72	0.19	31		0.00	6
TYC1900-1598-1	6.28	0.26	2	7.48	0.06	12	6.37	0.07	8		0.00	1	3.10	0.12	10	4.92	0.21	31	5.02	0.12	5
TYC1907-321-1	6.12	0.02	2	7.60	0.08	12	6.34	0.14	8		0.00	1	3.08	0.18	11	4.74	0.20	32		0.00	6
TYC1933-747-1	6.23	0.04	2	7.63	0.14	12	6.36	0.17	8		0.00	1	3.03	0.13	11	5.07	0.12	32		0.00	6
TYC1936-1174-1	6.10	0.03	2	7.25	0.07	12	6.08	0.10	8		0.00	1	2.88	0.10	10	4.85	0.09	24	4.66	0.12	5
TYC1942-1827-1	6.32	0.21	2	7.70	0.12	12	6.44	0.14	8	6.48	0.17	2	3.20	0.17	11	5.10	0.12	32		0.00	6
TYC1942-1827-1	6.56	0.01	2	7.51	0.12	12	6.33	0.14	8	6.45	0.32	2	3.19	0.17	11	4.97	0.18	32		0.00	6
TYC1951-1481-1	6.52	0.01	2	7.54	0.11	12	6.32	0.20	8	6.40	0.01	2	3.25	0.19	10	4.97	0.13	32		0.00	6
TYC1952-1819-1	6.44	0.07	2	7.52	0.13	12	6.31	0.19	8	6.26	0.04	2	3.20	0.11	11	4.96	0.15	31		0.00	6
TYC1954-529-1		0.00	0	7.37	0.17	11	6.08	0.34	6	6.11	0.04	2	2.93	0.17	10	4.79	0.28	17	4.78	0.16	6
TYC2455-727-1	6.36	0.05	2	7.41	0.10	12	6.24	0.05	8		0.00	1	3.11	0.10	11	4.97	0.10	32	4.89	0.18	6
TYC2473-1324-1	6.13	0.00	2	7.20	0.05	12	6.03	0.05	8		0.00	0	2.87	0.10	11	4.71	0.13	32	4.68	0.06	6
TYC2477-541-1		0.00	0	7.68	0.08	11	6.39	0.14	8	6.27	0.15	2	3.09	0.19	9	5.01	0.18	25		0.00	6
TYC2477-541-1	5.96	0.73	2	7.28	0.30	12	6.22	0.24	8		0.00	1	2.92	0.21	10	4.81	0.17	25	4.88	0.15	6
TYC2485-2097-1	6.18	0.08	2	7.33	0.20	12	5.99	0.28	8	6.07	0.06	2	2.91	0.14	10	4.58	0.19	29	4.60	0.08	6
TYC2488-121-1	6.27	0.09	2	7.34	0.09	12	5.95	0.20	8	6.04	0.22	2	2.91	0.14	11	4.62	0.14	32		0.00	6
TYC2488-849-1	6.27	0.10	2	7.60	0.11	12	6.45	0.17	8	6.45	0.08	2	3.20	0.20	10	4.94	0.26	29	5.13	0.18	6
TYC2490-1679-1		0.00	1	7.45	0.19	10	6.17	0.27	5		0.00	1	2.82	0.11	7	4.73	0.20	11		0.00	5
TYC2495-846-1	6.43	0.03	2	7.58	0.11	12	6.43	0.16	8	6.40	0.28	2	3.27	0.18	11	4.96	0.20	31		0.00	6
TYC2500-1087-1	6.19	0.03	2	7.27	0.38	12	6.19	0.14	8	6.22	0.07	2	3.05	0.18	10	4.75	0.19	22	4.92	0.06	5
TYC2507-1255-1	6.50	0.04	2	7.58	0.17	10	6.35	0.09	7	6.29	0.03	2	3.18	0.20	9	4.91	0.21	29	4.92	0.11	6
TYC2507-809-1	6.67	0.02	2	7.70	0.14	12	6.49	0.06	8	6.55	0.14	2	3.38	0.23	11	5.17	0.16	31	5.22	0.12	6
TYC2507-947-1	6.49	0.10	2	7.46	0.11	12	6.29	0.19	8	6.35	0.14	2	3.24	0.11	10	4.98	0.14	30	5.01	0.13	6
TYC2927-323-1	6.56	0.09	2	7.57	0.05	12	6.37	0.23	8		0.00	1	3.31	0.21	11	4.98	0.19	32		0.00	6
TYC2948-322-1	6.34	0.01	2	7.46	0.10	12	6.23	0.15	7	6.14	0.03	2	3.00	0.19	10	4.95	0.20	29		0.00	6
TYC2952-543-1	6.51	0.01	2	7.36	0.10	12	6.19	0.12	8	6.31	0.17	2	3.23	0.16	10	4.98	0.11	32		0.00	6
TYC2953-1958-1	6.44	0.02	2	7.54	0.05	12	6.34	0.07	8	6.27	0.14	2	3.23	0.15	11	4.94	0.15	32	5.01	0.09	6
TYC2957-1441-1	6.36	0.05	2	7.68	0.12	12	6.40	0.16	8		0.00	1	3.24	0.12	10	5.04	0.15	32		0.00	5
TYC2958-1173-1		0.00	1	7.48	0.14	12	6.21	0.14	8	6.18	0.17	2	3.04	0.24	10	4.73	0.26	25	4.73	0.13	6
TYC2961-1900-1	6.33	0.01	2	7.22	0.11	12	6.25	0.23	8		0.00	1	2.87	0.25	11	4.71	0.23	32	4.71	0.15	6
TYC2973-423-1	6.44	0.06	2	7.51	0.07	12	6.31	0.09	8	6.42	0.10	2	3.21	0.11	11	4.91	0.12	32	5.11	0.14	6
TYC2984-1187-1		0.00	1	7.08	0.06	12	5.89	0.10	7	5.91	0.00	2	2.64	0.11	10	4.66	0.20	21	4.61	0.07	6
TYC2991-699-1		0.00	1	7.40	0.10	12	6.13	0.13	7	6.04	0.03	2	2.97	0.12	9	4.66	0.17	16	4.86	0.13	6
TYC2991-699-2		0.00	0	7.39	0.09	12	6.27	0.10	8		0.00	1	2.84	0.14	9	4.89	0.11	16	4.87	0.14	6
TYC3396-2196-1	5.97	0.00	2	7.29	0.13	12	6.12	0.13	8		0.00	1	2.83	0.18	11	4.81	0.18	32		0.00	6
TYC3401-1647-1	6.13	0.09	2	7.39	0.12	12	6.04	0.17	7		0.00	1	2.78	0.18	8	4.84	0.13	19		0.00	6
TYC3415-2484-1	6.44	0.02	2	7.47	0.05	12	6.29	0.06	8		0.00	1	3.11	0.29	11	4.86	0.11	32	4.95	0.12	6
TYC3423-573-1	6.18	0.16	2	7.32	0.10	11	6.21	0.14	7		0.00	1	3.02	0.14	9	4.79	0.21	24	4.93	0.17	6
TYC3425-1596-1	6.18	0.05	2	7.23	0.11	12	6.15	0.27	8		0.00	0			1	4.80	0.20	11	4.81	0.11	32
TYC3425-1596-1	5.94	0.03	2	7.22	0.12	12	6.13	0.25	8		0.00	1	2.83	0.11	10	4.64	0.17	32		0.00	6
TYC3427-1400-1	6.21	0.04	2	7.48	0.11	12	6.42	0.13	8	6.34	0.28	2	3.17	0.19	11	4.95	0.18	32	4.94	0.13	6
TYC3796-306-1		0.00	1	7.35	0.16	10	6.19	0.18	8	6.29	0.05	2	3.08	0.20	10	4.73	0.20	27	4.76	0.13	6
TYC3797-247-1	6.43	0.02	2	7.61	0.12	12	6.33	0.16	8	6.18	0.18	2	3.14	0.21	11	4.77	0.15	29		0.00	6
TYC4133-206-1	6.27	0.03	2	7.24	0.13	12	6.17	0.26	8	6.29	0.30	2	2.91	0.20	11	4.84	0.21	32		0.00	6
TYC4133-256-1	6.46	0.14	2	7.31	0.18	12	6.24	0.28	8		0.00	0	3.06	0.10	11	4.97	0.15	32		0.00	6
TYC4142-1234-1	6.17	0.08	2	7.46	0.15	10	6.27	0.15	8		0.00	1	3.00	0.20	10	4.90	0.20	32		0.00	6
TYC4143-1061-1	6.50	0.16	2	7.31	0.36	12	6.26	0.30	8		0.00	1	2.95	0.18	11	4.98	0.15	32		0.00	6
TYC4152-127-1	6.56	0.01	2	7.66	0.14	12	6.17	0.26	8	6.38	0.13	2	3.01	0.10	11	4.91	0.16	32		0.00	6
TYC4152-1342-1	6.30	0.09	2	7.68	0.16	12	6.30	0.30	8	6.40	0.31	2	3.20	0.11	11	5.04	0.15	32	5.01	0.22	6

Continued on next page

Table 2 – continued from previous page

Tycho-2 ID	Al I			Si I			Ca I			Ca II			Sc II			Ti I			Ti II		
	A(Al I)	σ	N	A(Si I)	σ	N	A(Ca I)	σ	N	A(Ca II)	σ	N	A(Sc II)	σ	N	A(Ti I)	σ	N	A(Ti II)	σ	N
TYC4152-1342-1	6.36	0.10	2	7.41	0.20	12	6.28	0.30	8		0.00	1	3.11	0.14	11	5.05	0.14	32	4.85	0.13	6
TYC4152-569-1	6.43	0.15	2	7.63	0.25	11	6.25	0.14	8	6.39	0.16	2	3.14	0.17	11	4.94	0.17	30		0.00	6
TYC4152-569-1	6.53	0.12	2	7.42	0.21	12	6.38	0.32	8		0.00	1	3.09	0.14	11	4.96	0.18	32	4.92	0.22	6
TYC4159-1214-1	6.21	0.09	2	7.39	0.24	12	6.40	0.33	8		0.00	1	3.16	0.16	11	4.87	0.19	32	5.03	0.22	6
TYC4159-1294-1	6.28	0.18	2	7.35	0.28	12	5.98	0.24	8		0.00	1	2.88	0.19	11	4.64	0.19	32		0.00	6
TYC4159-1359-1	6.38	0.06	2	7.40	0.25	12	6.11	0.14	8		0.00	0	3.10	0.15	11	4.85	0.17	32		0.00	6
TYC4159-454-1	6.30	0.11	2	7.37	0.27	12	6.25	0.14	8		0.00	0	3.16	0.19	11	4.90	0.21	32		0.00	6
TYC4160-223-1	6.45	0.08	2	7.35	0.16	12	6.04	0.28	8	6.06	0.12	2	3.03	0.18	11	4.74	0.18	32		0.00	6
TYC4160-223-1	6.09	0.05	2	7.16	0.18	12	6.01	0.29	8		0.00	1	2.90	0.17	11	4.71	0.17	32		0.00	6
TYC4168-694-1	6.09	0.08	2	7.28	0.20	10	6.16	0.14	8		0.00	1	2.85	0.14	11	4.63	0.11	32		0.00	6
TYC4168-694-1	6.10	0.08	2	7.19	0.21	10	6.12	0.14	8		0.00	0	2.90	0.14	11	4.71	0.15	32		0.00	6
TYC4305-1262-1	6.26	0.13	2	7.42	0.20	12	6.40	0.31	8	6.31	0.19	2	3.05	0.15	11	4.95	0.14	31		0.00	6
TYC4305-1262-1	6.28	0.10	2	7.45	0.20	12	6.36	0.31	8	6.24	0.28	2	3.10	0.15	11	5.08	0.13	32		0.00	6
TYC4306-315-1	6.35	0.09	2	7.59	0.16	12	6.23	0.28	8		0.00	1	2.99	0.15	11	4.97	0.17	32		0.00	6
TYC4308-248-1	6.18	0.13	2	7.56	0.27	12	6.37	0.14	8	6.16	0.15	2	3.13	0.13	10	4.95	0.14	32	4.93	0.18	6
TYC4309-1078-1	6.30	0.42	2	7.51	0.18	12	6.15	0.28	8		0.00	1	3.05	0.16	11	4.73	0.12	32		0.00	6
TYC4318-2488-1	6.61	0.10	2	7.39	0.22	12	6.23	0.26	8	6.37	0.09	2	3.20	0.12	11	4.94	0.14	32		0.00	6
TYC4318-2488-1	6.43	0.05	2	7.38	0.30	12	6.20	0.26	8	6.35	0.22	2	3.17	0.17	11	4.90	0.19	32	5.00	0.14	6
TYC4320-2109-1		0.00	2	7.47	0.26	12	6.36	0.29	8	6.48	0.28	2	3.20	0.14	11	5.00	0.18	32		0.00	6
TYC4320-2109-1	6.56	0.06	2	7.71	0.14	12	6.30	0.24	8	6.26	0.19	2	3.14	0.13	11	4.85	0.18	32		0.00	6
TYC4321-805-1	6.22	0.11	2	7.25	0.15	12	6.16	0.27	8		0.00	1	2.93	0.20	11	4.88	0.18	32	4.81	0.18	6
TYC4321-839-1	6.40	0.12	2	7.28	0.18	12	6.27	0.30	8	6.14	0.02	2	2.90	0.14	11	4.91	0.16	32	4.95	0.22	6
TYC4322-1310-1	6.08	0.05	2	7.10	0.14	12	5.77	0.14	8		0.00	1	2.76	0.17	11	4.62	0.14	32	4.65	0.15	6
TYC4322-2075-1	6.45	0.11	2	7.61	0.22	12	6.36	0.28	8		0.00	1	3.26	0.14	11	5.05	0.17	32		0.00	6
TYC4323-1742-1	6.47	0.05	2	7.47	0.13	12	6.15	0.30	8	6.18	0.03	2	3.14	0.13	11	4.85	0.18	32		0.00	6
TYC4323-618-1	6.43	0.10	2	7.38	0.18	12	6.13	0.31	8	6.20	0.26	2	3.03	0.17	11	4.83	0.18	32		0.00	6
TYC4325-1243-1	6.31	0.08	2	7.33	0.18	12	6.26	0.29	8		0.00	1	3.14	0.18	11	5.05	0.16	32		0.00	6
TYC4325-1563-1	6.19	0.10	2	7.31	0.17	12	6.29	0.30	8		0.00	1	3.06	0.19	11	4.85	0.12	32		0.00	6
TYC4333-423-1	6.46	0.09	2	7.42	0.16	12	6.29	0.30	8		0.00	1	3.15	0.17	11	5.06	0.17	32		0.00	6
TYC4335-1122-1	6.25	0.10	2	7.49	0.25	11	6.32	0.14	8		0.00	1	3.10	0.15	11	4.93	0.20	32		0.00	6
TYC4335-2103-1	6.21	0.02	2	7.46	0.25	12	6.21	0.14	8		0.00	0	2.99	0.16	11	4.97	0.17	32		0.00	6
TYC4335-2105-1	6.41	0.04	2	7.43	0.20	12	6.38	0.28	8		0.00	1	3.15	0.19	11	4.93	0.18	32	5.06	0.19	6
TYC4336-886-1	6.28	0.06	2	7.20	0.24	11	6.04	0.14	8		0.00	1	2.79	0.15	11	4.55	0.14	32	4.57	0.18	6
TYC4338-1941-1	6.06	0.08	2	7.23	0.25	11	5.94	0.14	8		0.00	1	2.64	0.14	11	4.63	0.18	32	4.65	0.18	6
TYC4338-1942-1	6.35	0.11	2	7.36	0.18	12	6.10	0.14	8		0.00	0	3.05	0.12	11	4.87	0.14	32	4.69	0.17	6
TYC4338-647-1	6.37	0.09	2	7.33	0.25	12	6.33	0.14	8		0.00	0	3.03	0.10	11	4.80	0.13	32	4.87	0.22	6
TYC4339-2106-1	6.56	0.21	2	7.52	0.15	12	6.20	0.27	8		0.00	1	3.06	0.15	11	4.91	0.20	32		0.00	6
TYC4339-2273-1	6.12	0.08	2	7.13	0.11	12	6.15	0.27	8		0.00	1	2.77	0.16	11	4.75	0.16	32		0.00	6
TYC4339-2274-1	6.08	0.06	2	7.07	0.22	12	6.07	0.14	8		0.00	1	2.68	0.28	11	4.64	0.14	32		0.00	6
TYC4339-2274-1	6.04	0.07	2	7.07	0.18	11	6.06	0.14	8		0.00	1	2.62	0.28	11	4.66	0.11	32		0.00	6
TYC4341-343-1	5.84	0.08	2	7.17	0.19	12	5.88	0.14	8		0.00	0	2.67	0.13	11	4.53	0.19	32		0.00	6
TYC4341-936-1	6.31	0.16	2	7.28	0.14	12	6.12	0.14	8		0.00	0	2.94	0.12	10	4.84	0.13	32		0.00	6
TYC4346-356-1	6.33	0.08	2	7.35	0.12	12	6.20	0.24	8	6.18	0.04	2	3.13	0.18	11	4.92	0.16	32		0.00	6
TYC4347-1476-1	6.49	0.14	2	7.51	0.20	12	6.42	0.30	8	6.37	0.25	2	3.22	0.12	11	4.95	0.14	32		0.00	6
TYC4348-745-1	6.30	0.04	2	7.17	0.12	12	6.08	0.26	8	6.01	0.11	2	2.98	0.11	11	4.84	0.20	32	4.78	0.18	6
TYC4350-447-1	6.52	0.04	2	7.55	0.19	12	6.16	0.28	8	6.30	0.29	2	3.11	0.14	11	4.81	0.15	32	4.97	0.21	6
TYC4351-949-1	6.29	0.12	2	7.26	0.18	12	6.08	0.14	8		0.00	0	2.96	0.17	11	4.71	0.18	32	4.94	0.14	6
TYC4351-979-1	6.69	0.16	2	7.74	0.19	12	6.46	0.30	8		0.00	1	3.43	0.18	11	5.09	0.19	32		0.00	6
TYC4352-264-1	6.39	0.02	2	7.65	0.20	12	6.20	0.30	8		0.00	1	3.04	0.11	11	4.93	0.13	32		0.00	6
TYC4353-91-1	6.33	0.25	2	7.61	0.15	12	6.41	0.09	8		0.00	1	3.04	0.15	10	5.02	0.13	32	4.94	0.14	6
TYC4354-698-1	5.99	0.09	2	7.26	0.33	10	6.15	0.15	8		0.00	1	2.76	0.13	11	4.66	0.11	31		0.00	6
TYC4361-1793-1	6.36	0.13	2	7.36	0.15	12	6.34	0.30	8	6.29	0.23	2	3.04	0.16	11	4.98	0.17	32		0.00	6
TYC4361-1793-1	6.27	0.08	2	7.46	0.29	12	6.35	0.31	8		0.00	0	3.19	0.15	11	5.03	0.17	32		0.00	6
TYC4361-1793-1	6.34	0.08	2	7.46	0.29	12	6.35	0.31	8		0.00	0	3.12	0.15	11	4.99	0.17	32		0.00	6

booktabs longtable array pdflscape

Table 3 Orbital parameters of the sample stars.

Tycho-2 ID	e	R_{min} (kpc)	R_{max} (kpc)	Z_{min} (kpc)	Z_{max} (kpc)	$\|Z\|_{max}$ (kpc)	$\langle R \rangle$ (kpc)
TYC1381-1638-1	0.008	7.918	8.038	-0.090	0.090	0.090	7.978
TYC1383-84-1	0.336	8.023	16.157	-0.729	0.729	0.729	12.690
TYC1388-1791-1	0.127	6.488	8.375	-0.092	0.092	0.092	7.478
TYC1894-1961-1	0.075	7.930	9.222	-0.128	0.128	0.128	8.597
TYC1894-1961-1	0.075	7.930	9.222	-0.128	0.128	0.128	8.597
TYC1898-787-1	0.086	8.004	9.504	-0.360	0.360	0.360	8.780
TYC1898-2479-1	0.078	7.531	8.807	-0.082	0.081	0.082	8.186
TYC1899-1584-1	0.239	7.741	12.612	-0.365	0.366	0.366	10.431
TYC1900-1598-1	0.112	7.899	9.901	-0.290	0.289	0.290	8.942
TYC1907-321-1	0.189	7.616	11.156	-1.372	1.371	1.372	9.510
TYC1933-747-1	0.070	7.514	8.642	-0.047	0.047	0.047	8.092
TYC1936-1174-1	0.203	7.937	11.979	-0.336	0.336	0.336	10.126
TYC1942-1827-1	0.113	8.015	10.052	-0.287	0.288	0.288	9.081
TYC1942-1827-1	0.113	8.015	10.052	-0.287	0.288	0.288	9.081
TYC1951-1481-1	0.222	7.942	12.477	-0.079	0.079	0.079	10.432
TYC1952-1819-1	0.160	7.947	10.964	-0.321	0.321	0.321	9.564
TYC1954-529-1	0.116	8.028	10.133	-0.177	0.177	0.177	9.138
TYC2455-727-1	0.173	8.010	11.370	-0.204	0.204	0.204	9.818
TYC2473-1324-1	0.354	8.008	16.782	-2.265	2.267	2.267	13.011
TYC2477-541-1	0.275	4.574	8.046	-0.887	0.888	0.888	6.505
TYC2477-541-1	0.275	4.574	8.046	-0.887	0.888	0.888	6.505
TYC2485-2097-1	0.064	8.027	9.130	-0.312	0.312	0.312	8.594
TYC2488-121-1	0.344	8.078	16.556	-0.206	0.205	0.206	12.919
TYC2488-849-1	0.334	8.078	16.182	-1.393	1.393	1.393	12.692
TYC2490-1679-1	0.103	8.029	9.872	-0.382	0.381	0.382	8.982
TYC2495-846-1	0.217	8.008	12.438	-0.048	0.048	0.048	10.438
TYC2500-1087-1	0.143	6.152	8.211	-0.159	0.160	0.160	7.247
TYC2507-809-1	0.093	7.858	9.476	-0.297	0.297	0.297	8.691
TYC2507-947-1	0.132	7.878	10.281	-0.073	0.074	0.074	9.153
TYC2507-1255-1	0.145	7.935	10.634	-0.091	0.091	0.091	9.360
TYC2927-323-1	0.087	7.467	8.899	-0.160	0.160	0.160	8.206
TYC2948-322-1	0.335	7.981	16.014	-0.365	0.364	0.365	12.621
TYC2952-543-1	0.161	8.041	11.127	-0.938	0.938	0.938	9.665
TYC2953-1958-1	0.104	7.050	8.679	-0.223	0.223	0.223	7.893
TYC2957-1441-1	0.140	8.015	10.625	-0.042	0.045	0.045	9.395
TYC2958-1173-1	0.044	8.031	8.764	-0.114	0.114	0.114	8.403
TYC2961-1900-1	0.091	7.959	9.547	-0.147	0.147	0.147	8.784
TYC2973-423-1	0.239	8.022	13.058	-0.207	0.207	0.207	10.820
TYC2984-1187-1	0.255	4.768	8.026	-0.111	0.118	0.118	6.579
TYC2991-699-1	0.115	7.927	9.991	-0.039	0.038	0.039	9.003
TYC2991-699-2	0.104	7.885	9.708	-0.083	0.084	0.084	8.841
TYC3396-2196-1	0.406	7.799	18.449	-0.261	0.264	0.264	14.105
TYC3401-1647-1	0.097	6.716	8.166	-0.046	0.046	0.046	7.467
TYC3415-2484-1	0.084	7.017	8.299	-0.585	0.585	0.585	7.667
TYC3423-573-1	0.091	7.779	9.338	-0.154	0.153	0.154	8.589
TYC3425-1596-1	0.247	7.902	13.076	-0.853	0.852	0.853	10.775
TYC3425-1596-1	0.247	7.902	13.076	-0.853	0.852	0.853	10.775
TYC3427-1400-1	0.144	7.988	10.677	-0.398	0.398	0.398	9.412
TYC3796-306-1	0.177	5.764	8.237	-0.501	0.501	0.501	7.089
TYC3797-247-1	0.012	7.836	8.027	-0.037	0.037	0.037	7.932
TYC4133-206-1	0.248	8.073	13.408	-1.506	1.504	1.506	10.971
TYC4133-256-1	0.085	6.958	8.248	-0.259	0.259	0.259	7.622
TYC4142-1234-1	0.107	8.001	9.927	-0.054	0.055	0.055	9.002
TYC4143-1061-1	0.050	8.055	8.898	-0.160	0.160	0.160	8.485
TYC4152-127-1	0.137	7.627	10.050	-0.160	0.160	0.160	8.909

Continued on next page

Table 3 Orbital parameters of the sample stars (continued).

Tycho-2 ID	e	$R_{\min}$ (kpc)	$R_{\max}$ (kpc)	$Z_{\min}$ (kpc)	$Z_{\max}$ (kpc)	$\|Z\|_{\max}$ (kpc)	$\langle R \rangle$ (kpc)
TYC4152-569-1	0.061	7.353	8.309	-0.292	0.292	0.292	7.838
TYC4152-569-1	0.061	7.353	8.309	-0.292	0.292	0.292	7.838
TYC4152-1342-1	0.281	4.555	8.124	-0.497	0.497	0.497	6.561
TYC4152-1342-1	0.281	4.555	8.124	-0.497	0.497	0.497	6.561
TYC4159-454-1	0.230	7.704	12.297	-0.190	0.190	0.190	10.220
TYC4159-1214-1	0.045	7.921	8.662	-0.277	0.277	0.277	8.295
TYC4159-1294-1	0.045	7.612	8.326	-0.131	0.131	0.131	7.977
TYC4159-1359-1	0.245	7.774	12.807	-0.613	0.614	0.614	10.529
TYC4160-223-1	0.037	8.093	8.719	-0.149	0.149	0.149	8.410
TYC4160-223-1	0.037	8.093	8.719	-0.149	0.149	0.149	8.410
TYC4168-694-1	0.180	7.780	11.194	-0.276	0.276	0.276	9.613
TYC4168-694-1	0.180	7.780	11.194	-0.276	0.276	0.276	9.613
TYC4305-1262-1	0.090	7.161	8.571	-0.092	0.089	0.092	7.900
TYC4305-1262-1	0.090	7.161	8.571	-0.092	0.089	0.092	7.900
TYC4306-315-1	0.168	6.119	8.598	-0.180	0.180	0.180	7.452
TYC4308-248-1	0.069	8.483	9.750	-0.204	0.204	0.204	9.137
TYC4309-1078-1	0.125	7.803	10.024	-0.125	0.125	0.125	8.964
TYC4318-2488-1	0.083	7.976	9.422	-0.085	0.086	0.086	8.720
TYC4318-2488-1	0.083	7.976	9.422	-0.085	0.086	0.086	8.720
TYC4320-2109-1	0.114	7.856	9.868	-0.156	0.156	0.156	8.910
TYC4320-2109-1	0.114	7.856	9.868	-0.156	0.156	0.156	8.910
TYC4321-805-1	0.076	7.679	8.937	-0.197	0.197	0.197	8.334
TYC4321-839-1	0.273	5.372	9.397	-0.930	0.929	0.930	7.623
TYC4322-1310-1	0.288	6.336	11.457	-1.706	2.891	2.891	9.020
TYC4322-2075-1	0.082	7.354	8.663	-0.110	0.112	0.112	8.032
TYC4323-618-1	0.136	6.243	8.204	-0.342	0.342	0.342	7.277
TYC4323-1742-1	0.182	5.595	8.083	-0.206	0.206	0.206	6.939
TYC4325-1243-1	0.239	5.055	8.222	-0.234	0.234	0.234	6.814
TYC4325-1563-1	0.082	7.152	8.429	-0.071	0.071	0.071	7.813
TYC4333-423-1	0.146	7.358	9.872	-0.310	0.310	0.310	8.706
TYC4335-1122-1	0.233	5.284	8.487	-0.922	0.922	0.922	7.039
TYC4335-2103-1	0.074	7.947	9.223	-0.080	0.082	0.082	8.603
TYC4335-2105-1	0.087	7.489	8.910	-0.155	0.156	0.156	8.224
TYC4336-886-1	0.113	6.708	8.409	-0.182	0.182	0.182	7.601
TYC4338-647-1	0.269	5.249	9.115	-1.628	1.628	1.628	7.364
TYC4338-1941-1	0.077	7.337	8.565	-0.694	0.694	0.694	7.958
TYC4338-1942-1	0.077	8.040	9.376	-0.158	0.158	0.158	8.728
TYC4339-2106-1	0.030	7.887	8.375	-0.380	0.380	0.380	8.133
TYC4339-2273-1	0.283	4.814	8.618	-0.261	0.261	0.261	6.942
TYC4339-2274-1	0.179	6.660	9.572	-0.139	0.141	0.141	8.216
TYC4339-2274-1	0.179	6.660	9.572	-0.139	0.141	0.141	8.216
TYC4341-343-1	0.236	7.351	11.902	-4.663	4.661	4.663	9.461
TYC4341-936-1	0.075	7.538	8.762	-0.272	0.272	0.272	8.164
TYC4346-356-1	0.063	7.954	9.015	-0.250	0.250	0.250	8.498
TYC4347-1476-1	0.096	7.888	9.568	-0.536	0.536	0.536	8.755
TYC4348-745-1	0.075	7.027	8.172	-0.168	0.168	0.168	7.616
TYC4350-447-1	0.110	8.358	10.420	-0.246	0.246	0.246	9.441
TYC4351-949-1	0.232	5.259	8.439	-0.152	0.152	0.152	7.011
TYC4351-979-1	0.102	7.776	9.550	-0.134	0.134	0.134	8.694
TYC4352-264-1	0.085	8.024	9.523	-1.134	1.134	1.134	8.770
TYC4353-91-1	0.102	8.119	9.963	-0.329	0.329	0.329	9.080
TYC4354-698-1	0.223	5.540	8.712	-0.813	0.812	0.813	7.267
TYC4361-1793-1	0.134	8.076	10.567	-0.697	0.697	0.697	9.381
TYC4361-1793-1	0.134	8.076	10.567	-0.697	0.697	0.697	9.381
TYC4361-1793-1	0.134	8.076	10.567	-0.697	0.697	0.697	9.381

Table 4 Present day Galactic positions of the analysed stars.

Tycho2 ID	l (deg)	b (deg)	ϖ (mas)	R_{current} (kpc)	Z_{current} (kpc)
TYC1381-1638-1	205.3015	25.5308	40.8879	8.0195	0.0356
TYC1383-84-1	207.3015	28.3137	21.9803	8.0231	0.0465
TYC1388-1791-1	200.8102	25.9940	41.9916	8.0200	0.0355
TYC1894-1961-1	191.4101	11.4696	32.1855	8.0302	0.0311
TYC1894-1961-1	191.4101	11.4696	32.1855	8.0302	0.0311
TYC1898-787-1	189.6480	11.3422	29.0679	8.0341	0.0317
TYC1898-2479-1	190.4185	12.0639	57.4559	8.0167	0.0286
TYC1899-1584-1	190.0898	13.0681	21.9156	8.0432	0.0354
TYC1900-1598-1	191.4261	15.1521	39.3515	8.0260	0.0317
TYC1907-321-1	187.4376	15.3223	52.7712	8.0185	0.0300
TYC1933-747-1	193.2819	24.1475	44.6848	8.0155	0.0342
TYC1936-1174-1	195.7841	30.4668	54.8749	8.0081	0.0342
TYC1942-1827-1	201.2435	33.4380	28.3757	8.0265	0.0446
TYC1942-1827-1	201.2435	33.4380	28.3757	8.0265	0.0446
TYC1951-1481-1	204.5313	39.5117	16.2339	8.0430	0.0638
TYC1952-1819-1	203.7455	42.6321	10.0060	8.0641	0.0925
TYC1954-529-1	199.6082	42.8707	17.2899	8.0323	0.0646
TYC2455-727-1	184.9064	19.4185	36.6985	8.0261	0.0341
TYC2473-1324-1	189.3677	30.1452	46.3415	8.0130	0.0358
TYC2477-541-1	185.9123	30.5800	20.9271	8.0328	0.0495
TYC2477-541-1	185.9123	30.5800	20.9271	8.0328	0.0495
TYC2485-2097-1	194.7565	39.2651	18.0834	8.0263	0.0601
TYC2488-121-1	188.6096	38.6431	7.7315	8.0731	0.1056
TYC2488-849-1	190.5271	38.2945	36.5201	8.0156	0.0384
TYC2490-1679-1	185.7159	37.5857	13.3908	8.0426	0.0706
TYC2495-846-1	190.5283	42.1549	52.7709	8.0108	0.0395
TYC2500-1087-1	187.4274	46.0222	11.8473	8.0425	0.0857
TYC2507-809-1	186.3394	49.0593	15.3126	8.0266	0.0744
TYC2507-947-1	189.3948	48.5523	21.9494	8.0172	0.0588
TYC2507-1255-1	189.2609	48.6573	21.6013	8.0172	0.0591
TYC2927-323-1	175.3879	12.6135	21.2910	8.0485	0.0353
TYC2948-322-1	177.5052	20.6047	16.6148	8.0432	0.0464
TYC2952-543-1	175.8762	22.0413	14.7959	8.0510	0.0501
TYC2953-1958-1	172.3557	17.5241	60.2024	8.0158	0.0300
TYC2957-1441-1	180.3500	23.5847	30.8217	8.0261	0.0383
TYC2958-1173-1	180.6436	23.5461	15.4781	8.0517	0.0505
TYC2961-1900-1	177.9193	23.8819	32.8221	8.0249	0.0376

Tycho2 ID	l (deg)	b (deg)	ϖ (mas)	R_{current} (kpc)	Z_{current} (kpc)
TYC2973-423-1	182.2326	31.5021	20.9000	8.0285	0.0625
TYC2984-1187-1	184.5704	42.1966	24.1231	8.0195	0.0529
TYC2991-699-1	184.8919	44.9640	19.9768	8.0250	0.0605
TYC2991-699-2	184.8917	44.9637	19.6464	8.0254	0.0612
TYC3396-2196-1	170.3427	23.5149	59.3408	8.0156	0.0317
TYC3401-1647-1	168.3340	26.3536	49.0145	8.0141	0.0341
TYC3415-2484-1	174.4971	35.4189	45.5826	8.0127	0.0377
TYC3423-573-1	165.9433	39.5092	28.0040	8.0204	0.0479
TYC3425-1596-1	174.2266	46.0749	11.8163	8.0406	0.0858
TYC3425-1596-1	174.2266	46.0749	11.8163	8.0406	0.0858
TYC3427-1400-1	169.2339	41.1009	22.8618	8.0239	0.0580
TYC3796-306-1	165.1485	33.1532	11.2821	8.0433	0.0731
TYC3797-247-1	164.4031	35.7824	23.8746	8.0226	0.0500
TYC4133-206-1	147.9986	34.6148	4.8603	8.0906	0.1401
TYC4133-256-1	148.1490	34.0434	4.6979	8.0947	0.1453
TYC4142-1234-1	145.1461	40.5934	5.4635	8.0686	0.1450
TYC4143-1061-1	143.3263	42.6738	4.9402	8.0875	0.1620
TYC4152-127-1	136.5621	47.1189	6.7528	8.0587	0.1334
TYC4152-569-1	137.2592	47.5068	2.9316	8.1235	0.2764
TYC4152-569-1	137.2592	47.5068	2.9316	8.1235	0.2764
TYC4152-1342-1	135.7897	47.7040	7.4372	8.0546	0.1241
TYC4152-1342-1	135.7897	47.7040	7.4372	8.0546	0.1241
TYC4159-454-1	134.4946	47.7807	6.7438	8.0582	0.1344
TYC4159-1214-1	135.3916	48.2563	3.6503	8.1083	0.2294
TYC4159-1294-1	132.7837	48.9743	2.3081	8.1615	0.3526
TYC4159-1359-1	133.2040	48.9850	6.0383	8.0638	0.1517
TYC4160-223-1	131.9474	48.6954	5.4240	8.0701	0.1612
TYC4160-223-1	131.9474	48.6954	5.4240	8.0701	0.1612
TYC4168-694-1	122.1023	49.8765	3.0768	8.0885	0.2692
TYC4168-694-1	122.1023	49.8765	3.0768	8.0885	0.2692
TYC4305-1262-1	124.9661	10.1139	4.3307	8.1524	0.0655
TYC4305-1262-1	124.9661	10.1139	4.3307	8.1524	0.0655
TYC4306-315-1	120.2072	11.8252	6.1449	8.1151	0.0584
TYC4308-248-1	122.8976	10.6956	1.1989	8.6583	0.1799
TYC4309-1078-1	124.4803	11.1150	4.4280	8.1492	0.0686
TYC4318-2488-1	126.4010	10.4862	7.0771	8.0944	0.0507
TYC4318-2488-1	126.4010	10.4862	7.0771	8.0944	0.0507
TYC4320-2109-1	130.7048	11.5754	12.1338	8.0494	0.0415
TYC4320-2109-1	130.7048	11.5754	12.1338	8.0494	0.0415

Tycho2 ID	l (deg)	b (deg)	ϖ (mas)	$R_{\rm current}$ (kpc)	$Z_{\rm current}$ (kpc)
TYC4321-805-1	132.1521	12.1141	4.3383	8.1509	0.0733
TYC4321-839-1	132.5834	12.7144	5.5234	8.1208	0.0651
TYC4322-1310-1	127.8401	10.9261	4.2972	8.1478	0.0691
TYC4322-2075-1	126.4576	12.0923	7.3430	8.0975	0.0535
TYC4323-618-1	127.9197	11.2321	5.6995	8.1158	0.0593
TYC4323-1742-1	128.5815	12.0613	7.8150	8.0879	0.0518
TYC4325-1243-1	131.4995	12.4595	5.4702	8.1237	0.0643
TYC4325-1563-1	131.6214	12.6281	4.1270	8.1590	0.0780
TYC4333-423-1	139.3489	15.1181	4.3225	8.1318	0.0856
TYC4335-1122-1	135.7606	14.5127	3.9885	8.1609	0.0879
TYC4335-2103-1	135.8333	14.7139	4.1046	8.1547	0.0869
TYC4335-2105-1	135.8674	13.2857	5.4296	8.1185	0.0675
TYC4336-886-1	137.1981	15.5583	2.9483	8.1833	0.1163
TYC4338-647-1	133.6197	13.6262	3.5454	8.1768	0.0915
TYC4338-1941-1	132.5931	13.7553	3.7860	8.1654	0.0876
TYC4338-1942-1	133.0452	13.8404	3.7267	8.1687	0.0891
TYC4339-2106-1	134.2703	15.9711	3.6530	8.1651	0.1003
TYC4339-2273-1	133.8908	15.4979	4.5987	8.1414	0.0831
TYC4339-2274-1	134.8150	15.6531	3.3520	8.1816	0.1055
TYC4339-2274-1	134.8150	15.6531	3.3520	8.1816	0.1055
TYC4341-343-1	136.5801	18.0172	3.2200	8.1813	0.1208
TYC4341-936-1	136.8921	17.0495	2.1795	8.2523	0.1600
TYC4346-356-1	140.2982	16.1689	2.4964	8.2368	0.1364
TYC4347-1476-1	141.0998	18.0703	3.3609	8.1849	0.1176
TYC4348-745-1	143.1716	19.5898	5.4377	8.1215	0.0870
TYC4350-447-1	139.3581	18.1650	1.4933	8.3807	0.2342
TYC4351-949-1	140.9683	19.7857	5.5292	8.1189	0.0861
TYC4351-979-1	140.7552	18.9778	7.3500	8.0922	0.0692
TYC4352-264-1	141.4822	20.1466	4.8149	8.1401	0.0967
TYC4353-91-1	142.2693	23.4244	3.0202	8.1620	0.1565
TYC4354-698-1	137.7120	19.1671	4.4798	8.1502	0.0987
TYC4361-1793-1	146.2805	29.8070	5.8901	8.0886	0.1095
TYC4361-1793-1	146.2805	29.8070	5.8901	8.0886	0.1095
TYC4361-1793-1	146.2805	29.8070	5.8901	8.0886	0.1095